

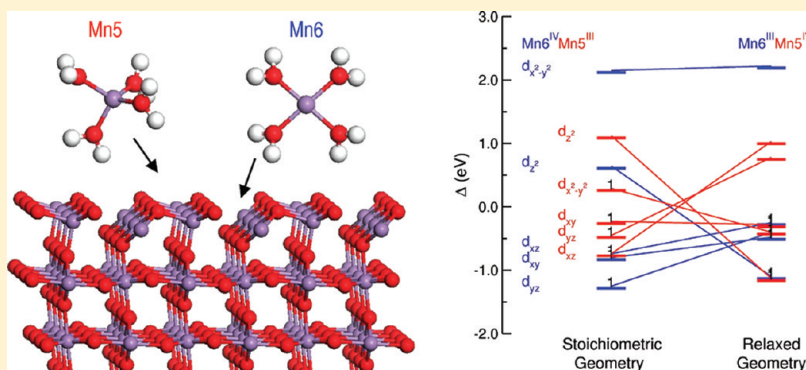
# First-Principles Calculations of Clean, Oxidized, and Reduced $\beta$ -MnO<sub>2</sub> Surfaces

Gloria A. E. Oxford\* and Anne M. Chaka

Physical Measurement Laboratory, National Institute of Standards and Technology, Gaithersburg, Maryland 20899, United States

Supporting Information

**ABSTRACT:** Stoichiometric and defective terminations of the  $\beta$ -MnO<sub>2</sub> (110), (100), and (101) surfaces are investigated as a function of oxygen partial pressure and temperature using ab initio thermodynamics. In agreement with studies on other rutile-type minerals, the (110) surface is predicted to be the most stable surface, followed by the (100) surface and then the (101) surface. The (110) and (101) surfaces are found to oxidize by formation of stable manganyl groups (Mn=O) at high oxygen chemical potentials, whereas the (100) surface is not likely to be oxidized under experimentally relevant conditions. All of the  $\beta$ -MnO<sub>2</sub> surfaces studied undergo reduction processes in UHV, resulting in many complicated structural changes. A number of the reduced surfaces exhibit new surface reconstructions not yet observed for any rutile-type mineral. Analysis of the dependence of manganese coordination geometry on oxidation state is carried out to facilitate understanding of the surface reconstructions. It is determined that the competition between optimizing d-orbital occupation and minimizing steric and repulsive electrostatic interactions drives the surface reconstructions observed for reduced  $\beta$ -MnO<sub>2</sub> surfaces. Symmetry-breaking at the surface allows for Jahn–Teller distortion of the reduced Mn<sup>III</sup> coordination sphere for some surface reconstructions.



## INTRODUCTION

Manganese oxides and hydroxides are found in many geological settings and occur in the form of more than 30 minerals.<sup>1</sup> They participate in a variety of redox and acid/base reactions in the environment because they form interfacial barriers on soils and sediments in marine and freshwater environments and on rock and other mineral surfaces. The ability of manganese oxides to adsorb and oxidize heavy metal pollutants, such as chromium and arsenic, has been recognized for decades. Because of their ubiquity in the environment and their reactivity, these minerals serve as an important control in regulating the concentrations of groundwater contaminants. Manganese oxides are also commercially relevant as the cathode material in alkaline batteries<sup>2,3</sup> and have been studied for use in catalytic applications<sup>4–6</sup> and water treatment media.<sup>7,8</sup> Their redox behavior indicates that manganese oxides may potentially act as sensors as well.<sup>9</sup>

Despite the importance of manganese oxides in geochemical processes and in technological applications, their surface structures and properties have not been well studied. For example, recent reports indicate that manganese oxides can oxidize Cr<sup>III</sup> to toxic Cr<sup>VI</sup><sup>10–17</sup> and toxic As<sup>III</sup> to As<sup>V</sup>.<sup>18–22</sup> Although these studies aimed at understanding the role of manganese oxides in the oxidation of heavy metals, it remains unclear which manganese species participate in the process and which

manganese oxide surfaces are relevant for redox chemistry. A fundamental knowledge of the surface structures and their redox properties at environmentally relevant conditions is the necessary groundwork to be laid before complex interactions between heavy metal ions and manganese oxide surfaces can be fully delineated.

A small number of studies have examined manganese oxide surfaces. The earliest work demonstrated reduction<sup>23</sup> and oxidation<sup>24</sup> of manganese oxide surfaces using X-ray photoelectron spectroscopy (XPS). The surface structures, however, were not characterized in either study. More recently, Langell et al.<sup>25</sup> examined the MnO (100) surface using high-resolution electron energy loss spectroscopy (EELS) and showed that oxidation of the surface leads to the formation of Mn<sub>2</sub>O<sub>3</sub> and subsequently Mn<sub>3</sub>O<sub>4</sub>. Intermixture of the oxide species prevented isolation of pure-phase layers and hence structural determination of the surface. EELS in scanning transmission electron microscopy was also used to analyze manganese valence at the surfaces of natural manganese oxides.<sup>26</sup> It was found that the average valence at the  $\beta$ -MnO<sub>2</sub> surface was 4.0, in agreement with the formal

Received: April 20, 2011

Revised: July 7, 2011

Published: July 14, 2011

valence. A few studies have investigated thin films of  $\beta$ - $\text{MnO}_2$ , a rutile-type mineral also known as pyrolusite, grown on other oxide surfaces. Chambers and Liang<sup>27</sup> used low-energy electron diffraction and reflection high-energy electron diffraction (RHEED) to demonstrate that up to six bilayers of  $\beta$ - $\text{MnO}_2$  can be grown epitaxially on the rutile  $\text{TiO}_2$  (110) surface. A second phase was introduced into thicker films as the structural effect of the  $\text{TiO}_2$  substrate diminished, making it difficult to fabricate well-characterized surfaces.  $\beta$ - $\text{MnO}_2$  films were also grown epitaxially on  $\text{LaAlO}_3$  and  $\text{MgO}$  (001) surfaces as determined with RHEED and had some oxygen deficiencies indicated by XPS.<sup>28</sup> The molecular-level surface structure was not discussed.

Recently, a few computational studies have investigated manganese oxide surfaces on a molecular level. Using the generalized gradient approximation (GGA) to the exchange-correlation functional in density functional theory (DFT) and ab initio thermodynamics, Franchini et al.<sup>29</sup> explored various reconstructions of the  $\text{MnO}$  (111) surface and predicted their relative thermodynamic stabilities at different oxygen chemical potentials. The stabilization of the polar surface was explained in terms of structural and electronic changes in the outermost layers of the surface. GGA calculations, semiempirical electronic-structure methods, and molecular dynamics were applied to study the interaction between water and the (010) surface of  $\gamma$ - $\text{MnOOH}$ .<sup>30</sup> This work predicted physisorption of water on the surface with no ordering. Ngoepe and co-workers<sup>31</sup> used atomistic simulations based on rigid-ion interatomic potentials to characterize low index surfaces of  $\beta$ - $\text{MnO}_2$  and ramsdellite, another  $\text{MnO}_2$  polymorph.

Given the large number of possible manganese oxide surfaces and the lack of detailed structural analyses on them, very little of the surface structure is known at an atomic level. Because surface structure and composition are intimately related to the reactivity of mineral surfaces,<sup>32</sup> understanding surface reconstructions and manganese redox behavior at oxide surfaces would aid the development of accurate geochemical models and more efficient manganese oxide batteries and catalysts. DFT offers an effective means to investigate surface structures and properties. It has successfully been applied to calculate surface structures and energies and to explain experimentally observed surface reconstructions.<sup>33–39</sup> In this work, the (110), (100), and (101) surfaces of  $\beta$ - $\text{MnO}_2$  are examined using periodic DFT calculations. This polymorph of  $\text{MnO}_2$  is the most stable and is commonly found in natural deposits throughout the world. It is also a major component in batteries.  $\beta$ - $\text{MnO}_2$  has a rutile-type structure constructed from single chains of edge-sharing  $\text{Mn}^{\text{IV}}\text{O}_6$  octahedra running along the [001] direction and linked by shared corners.  $\beta$ - $\text{MnO}_2$  falls in the  $P4_2/mnm$  space group with  $a = 4.4041 \text{ \AA}$  and  $c = 2.8765 \text{ \AA}$ .<sup>40</sup> Although a previous computational study described stoichiometric surfaces of  $\beta$ - $\text{MnO}_2$ ,<sup>31</sup> it treated the manganese and oxygen atoms with rigid-ion interatomic potentials and could not address redox behavior and its structural consequences. The electronic structure of the manganese atoms is expected to affect the surface reconstructions, and the manganese and oxygen atoms can be expected to experience covalent interactions. An electronic structure method, such as DFT, must be used to successfully model these factors influencing structure, particularly with respect to defects, multiple oxidation states, and reconstructions that are outside the range of parameterization feasible for empirical pair potentials. This work also considers oxidized and reduced  $\beta$ - $\text{MnO}_2$  surfaces in an effort to understand

the redox behavior of stable surface cleavages. New surface reconstructions that differ markedly from known surface reconstructions of other rutile-type minerals are discussed. The relationship between manganese d-orbital occupation and coordination geometry is an important driver in these new surface reconstructions.

## METHODS

**1. Density Functional Theory Calculations.** Periodic DFT calculations were performed with GGA as formulated by Perdew, Burke, and Ernzerhof (PBE).<sup>41</sup> A double-numeric-plus-polarization, atom-centered basis set was used in the calculations, which were carried out with the DMol<sup>3</sup> software.<sup>42–44</sup> For bulk lattice optimizations, energies were well converged with  $(4 \times 4 \times 7)$   $k$  points in a Monkhorst–Pack grid<sup>45</sup> and a 4.5  $\text{\AA}$  real-space cutoff. Although  $\beta$ - $\text{MnO}_2$  has been shown to exhibit an antiferromagnetic helical spin arrangement,<sup>46,47</sup> an idealized collinear arrangement was modeled in this study, as has been done in previous studies.<sup>2,48,49</sup> Lattice constant optimization was performed for the antiferromagnetic (AFM), ferromagnetic (FM), and nonmagnetic (NM) states of  $\beta$ - $\text{MnO}_2$ . The AFM state is found to be the ground state, in agreement with experimental results.<sup>46,47</sup> It lies 97 and 648 meV per formula unit lower in energy than the FM and NM states, respectively. The optimized bulk lattice constants of 4.4569  $\text{\AA}$  (+1.2%) and 2.8823  $\text{\AA}$  (+0.2%) for the AFM state are in excellent agreement with experimental values (percent error shown in parentheses)<sup>40</sup> and similar to results from other GGA studies.<sup>48,49</sup> The Mulliken and Hirshfeld local spin magnetic moments on the manganese atoms are 2.59  $\mu_B$  and 2.40  $\mu_B$ , respectively, and are higher than the long-range ordering magnetic moment of 2.34  $\mu_B$  determined experimentally at 13 K, in agreement with a previous GGA study.<sup>49</sup>

Although the band gap of  $\beta$ - $\text{MnO}_2$  has been determined to be 1.0 eV,<sup>50</sup> the DFT self-interaction error leads to an inability to open the band gap, and metallic behavior is predicted by the PBE functional with 0.17 states/eV at the Fermi level. Hence, a more in-depth discussion of functionals is warranted. Hybrid functionals and the DFT+U approach<sup>51</sup> have been used to open band gaps in calculations on some materials, but only hybrid functionals did so for  $\beta$ - $\text{MnO}_2$ .<sup>49</sup> Hybrid functionals, however, tend to favor oxygen-poor compounds, leading to incorrect trends in calculated relative formation energies for various manganese oxides<sup>49</sup> and endothermic oxygen insertion energies in bulk  $\text{UO}_2$ ,<sup>52</sup> which is known to prefer hyperstoichiometry and readily forms  $\text{UO}_{2.25}$  (DFT+U also has the same problem).<sup>49,53</sup> GGA, in contrast, has successfully modeled the energetics of these systems. Given these results and the lack of validation of these methods in predicting stable reconstructions, it is unclear whether hybrid functionals and DFT+U are reliable methods for calculating surface energies and chemical potentials. In our experience, we have found better agreement with experimental temperature and pressure thresholds for surface oxidation and reduction reactions for metal oxides when the Hubbard U correction was not included.<sup>54–56</sup> It has been shown, for example, that while GGA predicted an oxygen chemical potential for transition to a ferryl-terminated  $\alpha$ - $\text{Fe}_2\text{O}_3$  (0001) surface in quantitative agreement with experiments,<sup>56</sup> the DFT+U approach calculated the structural transition to occur at an unphysically high oxygen chemical potential.<sup>55</sup> Therefore, for the purposes of

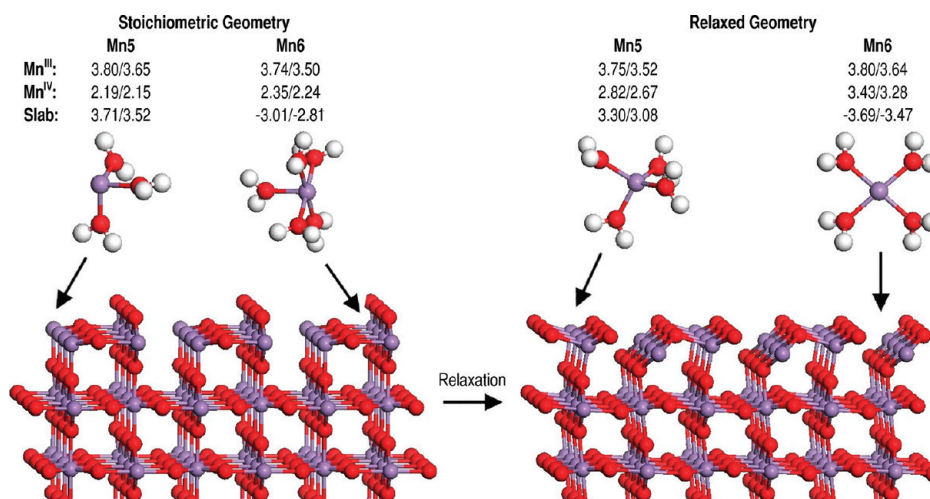


**Figure 1.** Illustration of  $\text{Mn}(\text{H}_2\text{O})_x$  molecular complexes used to calibrate Mulliken and Hirshfeld charge populations and to calculate d-orbital energies for the  $\beta\text{-MnO}_2$  (110)  $\text{O}_s$ -half surface. Manganese and oxygen atoms are fixed at positions observed in the optimized slab. Hydrogen atom positions are optimized. The Mulliken and Hirshfeld spins calculated for the Mn5 and Mn6 molecular complexes in the 3+ and 4+ oxidation states are shown along with those calculated for Mn5 and Mn6 in the slab. The first value is the Mulliken spin, and the second value is the Hirshfeld spin. The slabs are viewed along the [001] direction. (O, red/dark sphere; Mn, purple/light sphere; H, white sphere).

this work when our focus is on surface structure and redox reactions rather than on optical properties or conductivity, we do not include the Hubbard  $U$  parameter in our DFT calculations, nor do we use hybrid functionals.

Calculations on the (110), (100), and (101) surfaces were performed on periodic slabs starting with the AFM state. A total vacuum space of at least 10 Å was used between slabs and was verified to be large enough to avoid interactions between slabs; surface energies differed by less than 0.1 meV/Å<sup>2</sup> when the total vacuum space was increased to 30 Å. The real-space cutoff was reduced to 3.5 Å for the surface calculations to improve computational efficiency, which introduced no more than a 2 meV/Å<sup>2</sup> variation in the surface energies when compared with the converged 5.0 Å cutoff. Converged (7 × 4 × 1), (1 × 4 × 7), and (4 × 4 × 1) Monkhorst–Pack grids were used for the (110), (100), and (101) surfaces, respectively. Some ordered oxygen vacancies were modeled with (1 × 2), (2 × 1), or (2 × 2) surface cells. For these calculations, the number of  $k$  points along the direction of two unit cell lengths was reduced from four to two or from seven to four. The surfaces were related by inversion symmetry, and a force tolerance of 0.01 eV/Å was employed during optimization of all atoms in the slab. For the (110) surface, convergence of the surface energies and of the middle of the slab to bulk-like geometries was achieved with five metal layers. The (100) and (101) surfaces required seven metal layers. Frequency calculations were performed in DMol<sup>3</sup> using a frozen phonon method<sup>57</sup> with atom displacements of ±0.01  $a_0$  in each direction.

The oxidation state of surface manganese atoms was established using Mulliken and Hirshfeld charges and spins. Although charge partitioning by the Mulliken and Hirshfeld methods is not exact and provides relative oxidation states at best, the spin moments are particularly useful because they reveal the number of unpaired d electrons on the manganese atoms. To facilitate chemical understanding of the surface reconstructions, a series of molecular complexes analogous to surface coordination geometries observed in the periodic slab were constructed. By assigning formal oxidation states to the constructed  $\text{Mn}(\text{H}_2\text{O})_x$  molecular complexes and calculating the Mulliken and Hirshfeld populations,

the spins on the surface manganese in the slabs were calibrated (see Figure 1 for an illustration of the calibration procedure; details are discussed later in context of the specific surface).

**2. Ab Initio Thermodynamics.** Ab initio thermodynamics provides a framework for comparing surface free energies of surfaces with varying stoichiometries under different temperature and pressure regimes, linking ab initio calculations to environmentally relevant conditions. It has been applied to understand surface reconstructions and redox behavior of a variety of metal oxide surfaces.<sup>33–35,37,39,58–65</sup> A thorough treatment of the theory is provided by Reuter and Scheffler.<sup>34</sup> Here, the details are summarized in the context of the  $\beta\text{-MnO}_2$  surfaces.

For a slab with two equivalent surfaces in contact with a gas reservoir, the surface free energy  $\gamma(T, p)$  is defined as

$$\gamma(T, p) = \frac{1}{2A} \left\{ G_{\text{slab}}(T, p, N_i) - \sum_i N_i \mu_i(T, p) \right\} \quad (1)$$

where  $A$  is the surface area,  $G_{\text{slab}}$  is the Gibbs free energy of the slab,  $N_i$  is the number of type  $i$  atoms, and  $\mu_i$  is the chemical potential of type  $i$  atoms. The Gibbs free energy of the slab is obtained from the DFT calculations. At pressures below 101 bar, the Gibbs free energy is approximately equal to the Helmholtz free energy.<sup>34</sup> The Helmholtz free energy at 0 K is equal to the internal energy, which is the DFT total energy of the slab, neglecting the zero point energy. The vibrational energy (including the zero point energy) and entropy contributions to the Gibbs free energy at different temperatures are calculated using the vibrational partition function and the fundamental relationships of statistical thermodynamics, giving

$$\Delta G^{\text{vib}} = k_B \sum_i \Theta_{v_i} \left( \frac{1}{2} + \frac{1}{e^{\Theta_{v_i}/T} - 1} \right) - k_B T \sum_i \left[ \frac{\Theta_{v_i}/T}{e^{\Theta_{v_i}/T} - 1} - \ln(1 - e^{-\Theta_{v_i}/T}) \right] \quad (2)$$

where  $k_B$  is the Boltzmann constant, the summation is over all

vibrational frequencies  $\nu_i$ , and  $\Theta = h\nu_i/k_B$ . Here,  $h$  is Planck's constant.

For the  $\beta$ -MnO<sub>2</sub> system,  $\mu_{\text{Mn}}$  and  $\mu_{\text{O}}$  enter into eq 1. Assuming the bulk material acts as a thermal reservoir and the surface, gas reservoir, and bulk oxide are in chemical equilibrium,  $\mu_{\text{Mn}}$  and  $\mu_{\text{O}}$  are related to the Gibbs free energy of the components in the system:

$$\mu_{\text{Mn}} + 2\mu_{\text{O}} = G_{\text{MnO}_2}^{\text{bulk}} \quad (3)$$

$$\mu_{\text{O}} = \frac{1}{2} G_{\text{O}_2}^{\text{gas}} \quad (4)$$

where  $G_{\text{MnO}_2}^{\text{bulk}}$  and  $G_{\text{O}_2}^{\text{gas}}$  are the Gibbs free energies of the bulk oxide per formula unit and of an O<sub>2</sub> molecule, respectively. The independent variable in this system is  $\mu_{\text{O}}$ . As discussed elsewhere,<sup>34</sup> physical constraints on  $\mu_{\text{O}}$  lead to limits on the range of accessible  $\mu_{\text{O}}$  values. The maximum allowable  $\mu_{\text{O}}$  occurs when gas-phase oxygen condenses on the surface and is computed using eq 4. In oxygen-poor conditions,  $\mu_{\text{O}}$  reaches a minimum when MnO<sub>2</sub> separates into bulk manganese metal and gas-phase oxygen:

$$\mu_{\text{O},\text{min}} = \frac{1}{2} (G_{\text{MnO}_2}^{\text{bulk}} - G_{\text{Mn}}^{\text{bulk}}) \quad (5)$$

where  $G_{\text{Mn}}^{\text{bulk}}$  is the Gibbs free energy of bulk manganese metal per atom. Rescaling  $\mu_{\text{O},\text{max}}$  to zero gives the following range of accessible  $\mu_{\text{O}}$  values:

$$\frac{1}{2} \Delta G_{f,\text{MnO}_2} < \mu_{\text{O}} - \frac{1}{2} G_{\text{O}_2}^{\text{gas}} < 0 \quad (6)$$

where  $\Delta G_{f,\text{MnO}_2}$  is the Gibbs free energy of formation of the oxide. At 0 K, the DFT total energies of O<sub>2</sub> and of the bulk oxide and bulk metal are used to calculate  $\mu_{\text{O},\text{max}}$  and  $\mu_{\text{O},\text{min}}$ , respectively. The DFT total energy of manganese metal was calculated for collinear AFM  $\alpha$ -Mn using GGA optimized lattice constants from the literature<sup>66</sup> and a  $4 \times 4 \times 4$  Monkhorst–Pack<sup>45</sup> grid. Although AFM  $\alpha$ -Mn exhibits a complex, noncollinear spin arrangement, it has been shown by Hobbs and co-workers<sup>66</sup> that collinear and noncollinear arrangements are essentially degenerate at the optimized lattice constants.

For the MnO<sub>2</sub> system, eq 1 can be rewritten as

$$\gamma(T, p) = \frac{1}{2A} \left\{ E_{\text{slab},0\text{K}} + \Delta G^{\text{vib}} - N_{\text{Mn}} G_{\text{MnO}_2}^{\text{bulk}}(T, p) + (2N_{\text{Mn}} - N_{\text{O}}) \mu_{\text{O}}(T, p) \right\} \quad (7)$$

The enthalpic and entropic contributions to  $G_{\text{MnO}_2}^{\text{bulk}}$  at different temperatures are calculated using eq 2, since the relevant experimental data are not available. The temperature dependence of  $\mu_{\text{O}}$  is determined using the NIST-JANAF tables<sup>67</sup> for gas-phase O<sub>2</sub> at standard pressure, and  $\mu_{\text{O}}$  at different pressures is calculated using

$$\mu_{\text{O}}(T, p) = \mu_{\text{O}}(T, p^{\circ}) + \frac{1}{2} kT \ln \left( \frac{p}{p^{\circ}} \right) \quad (8)$$

It is essential to assess the errors associated with the methodology employed in these calculations. As discussed previously, the calculated bulk properties of  $\beta$ -MnO<sub>2</sub> have been found to be

in good agreement with experimental data. There exist no data on the surface properties as far as we have determined with which to compare the calculations. Yet, cancellation of errors in DFT energies can be evaluated by calculating  $\Delta G_f$  for the bulk oxide at 0 K. Because  $\Delta G_f$  is equal to the enthalpy of formation  $\Delta H_f$  at 0 K and few thermochemical data exist for MnO<sub>2</sub>, the experimental value of  $\Delta H_f$  at 0 K was determined to be  $-5.34$  eV<sup>67–69</sup> using

$$\begin{aligned} \Delta H_{f,\text{MnO}_2}^{\circ}(298.15 \text{ K}) - \Delta H_{f,\text{MnO}_2}^{\circ}(0 \text{ K}) &= \left\{ H_{\text{MnO}_2}^{\circ}(298.15 \text{ K}) \right. \\ &- \left. H_{\text{MnO}_2}^{\circ}(0 \text{ K}) \right\} - \left\{ H_{\text{Mn}}^{\circ}(298.15 \text{ K}) - H_{\text{Mn}}^{\circ}(0 \text{ K}) \right\} \\ &- \left\{ H_{\text{O}_2}^{\circ}(298.15 \text{ K}) - H_{\text{O}_2}^{\circ}(0 \text{ K}) \right\} \quad (9) \end{aligned}$$

where  $H_{\text{MnO}_2}^{\circ}$ ,  $H_{\text{Mn}}^{\circ}$ , and  $H_{\text{O}_2}^{\circ}$  are the enthalpies of bulk MnO<sub>2</sub>,  $\alpha$ -Mn, and gaseous O<sub>2</sub>, respectively. The calculated value of  $\Delta H_f$  underestimates the experimental value by 6.7%. The error results from uncertainties in the O<sub>2</sub>, MnO<sub>2</sub>, and  $\alpha$ -Mn DFT energies. Modeling the O<sub>2</sub> molecule is problematic for DFT because of the short bond length and triplet ground state. In this work, the PBE error in the O<sub>2</sub> atomization energy is 0.90 eV per O<sub>2</sub> molecule when using the same basis set and cutoff radius as used for the periodic DFT calculations. This value is similar to those found in other DFT studies.<sup>39,41</sup> To correct for this error, 0.90 eV was added to the DFT total energy of the O<sub>2</sub> molecule, as has been done in previous work.<sup>39,58</sup> The use of an O<sub>2</sub> energy correction here leads to an overestimation of  $\Delta H_f$  by 10.2%, indicating that the errors in the MnO<sub>2</sub> and  $\alpha$ -Mn energies cancel some of the error in the O<sub>2</sub> energy. However, as noted by Franchini et al.,<sup>49</sup> an O<sub>2</sub> energy correction generally improves agreement between calculated and experimental formation energies of manganese oxides. For our purposes, the uncertainty in the  $\alpha$ -Mn calculations likely due to the use of a collinear spin arrangement in place of the complex noncollinear spin arrangement affects only the oxygen-poor region of  $\mu_{\text{O}}$ . Although the error in formation enthalpy is higher when the O<sub>2</sub> correction is employed in our calculations, its use allows us to anchor the upper limit of  $\mu_{\text{O}}$  to the experimental O<sub>2</sub> atomization energy and therefore provides more accurate energies in the upper range of  $\mu_{\text{O}}$ , which is the environmentally relevant range.

## RESULTS

**1. (110) Surface.** Of the three  $\beta$ -MnO<sub>2</sub> surfaces studied here, the (110) surface is the most stable, in agreement with GGA investigations of other rutile-type surfaces.<sup>35,38,70</sup> The stoichiometric surface shown in Figure 2a consists of two types of manganese: one 5-fold coordinated (Mn5) and one 6-fold coordinated (Mn6). Mn6 atoms form rows along the [001] direction connected by bridging oxygen atoms (O<sub>br</sub>). In the same plane as Mn5 and Mn6 are 3-fold coordinated surface oxygen atoms (O<sub>s</sub>). On the stoichiometric surface, Mn5 and Mn6 have Mulliken spins of 2.70 and  $-2.52$ , respectively. These spins are comparable to the Mulliken spin of 2.59 on Mn<sup>IV</sup> in the bulk and are therefore consistent with high-spin Mn<sup>IV</sup> at the surface. The calculated vertical layer spacings  $d$  and lateral relaxations are listed in Tables 1 and 2, respectively (see Figure 2b for a depiction of the layer sequence). Both O<sub>br</sub> and Mn5 experience modest inward relaxations of  $-8\%$  to  $-9\%$ , whereas O<sub>s</sub> and Mn6 relax out of the surface by  $+12\%$  and  $+7\%$ , respectively, relative to the bulk. Although the direction of relaxation of the manganese atoms agrees with a previous study using interatomic potentials,<sup>31</sup>

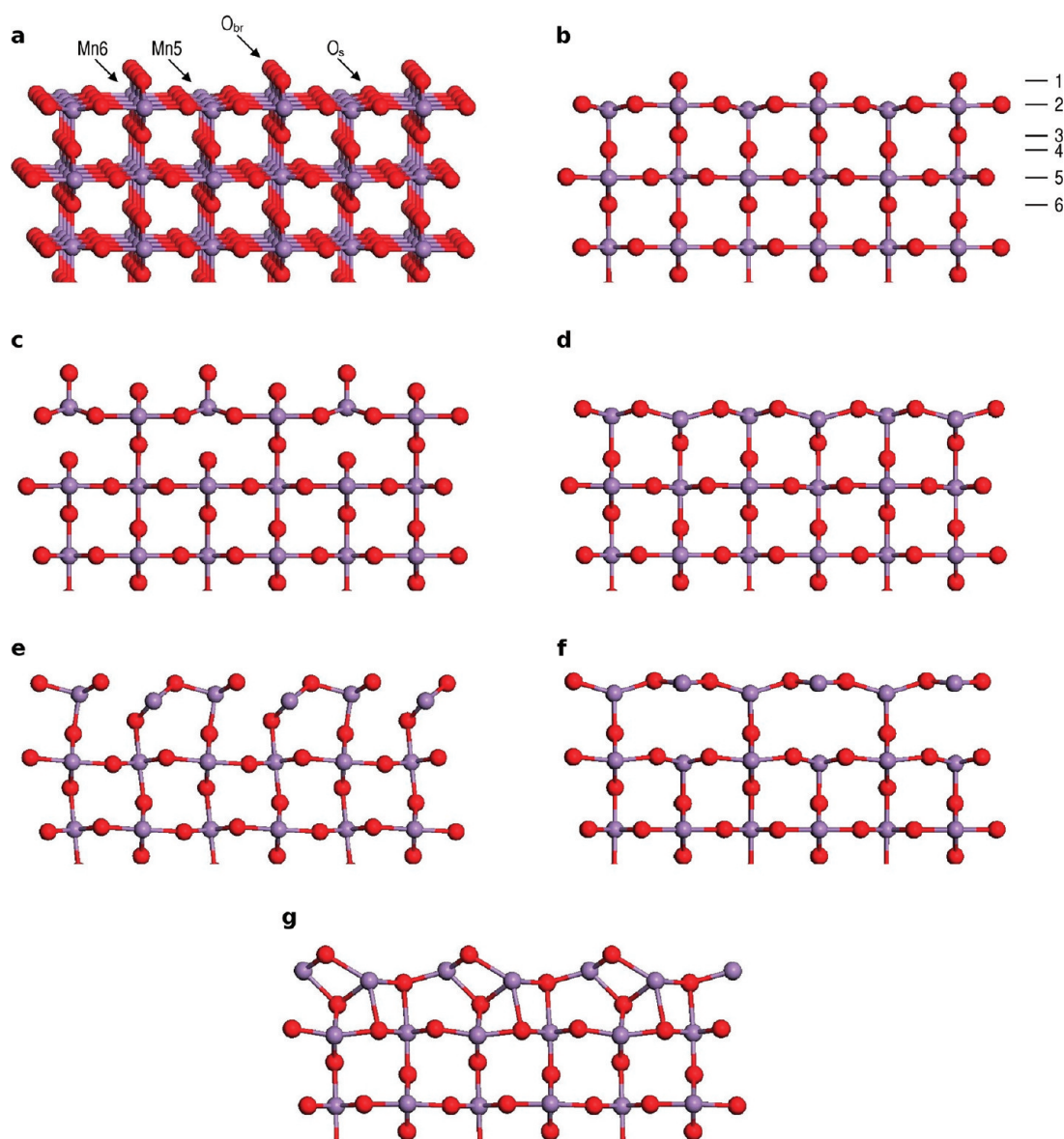


**Figure 2.** (a)  $\beta$ -MnO<sub>2</sub> (110) stoichiometric surface showing surface atom types. Stable (110) surface terminations viewed along the [001] direction: (b) stoichiometric showing layer stacking sequence; (c) manganyl; (d) O<sub>br</sub>-all; (e) O<sub>s</sub>-half; (f) O<sub>s</sub>-all; (g) O<sub>s</sub>-half/O<sub>br</sub>-all (O, red/dark sphere; Mn, purple/light sphere).

the inward relaxation of O<sub>br</sub> does not. This discrepancy may be due to the use of rigid-ion potentials in the previous study that do not account for the electronic structure of the oxide material. Most atoms undergo small lateral relaxations along the  $[1\bar{1}0]$  direction (Table 2), with O<sub>s</sub> atoms moving away from Mn6 (Table 2). These calculated relaxations are predictive because of the lack of experimental data for  $\beta$ -MnO<sub>2</sub> surfaces. Comparison with other rutile-type systems demonstrate that the vertical relaxations for the first two layers are reasonably consistent with experiments<sup>71,72</sup> and other GGA<sup>36,63,73–75</sup> and LDA<sup>76</sup> studies of TiO<sub>2</sub> and SnO<sub>2</sub>. Although the reported O<sub>br</sub> relaxations are inconsistent between these studies, it is generally thought that O<sub>br</sub> experiences inward relaxation,<sup>77</sup> in agreement with the observed relaxation of O<sub>br</sub> here. Only the O<sub>s</sub> atoms relax along the  $[1\bar{1}0]$  direction in the studies on other rutile-type metal oxides.

*Ab Initio Thermodynamics.* Fourteen (110) surface terminations with additional oxygen atoms or oxygen and manganese vacancies were investigated to determine their stabilities as a function of oxygen chemical potential ( $\mu_{\text{O}}$ ). The most interesting lowest energy surfaces are shown in Figure 2. The surface energies  $\gamma$  at 0 K are plotted as a function of  $\mu_{\text{O}}$  in Figure 3 for the stoichiometric surface and eight stable surfaces, which are designated as follows. The manganyl surface has one additional oxygen atom per unit surface cell that completes the coordination sphere of Mn5, forming a manganyl (Mn=O) group on the surface (Figure 2c). Surfaces with varying concentrations of O<sub>br</sub> vacancies are denoted O<sub>br</sub>-quarter for one O<sub>br</sub> vacancy in a  $2 \times 2$  surface cell, O<sub>br</sub>-half(a) for the surface with every other O<sub>br</sub> atom removed, O<sub>br</sub>-half(b) for the surface with every other row of O<sub>br</sub> atoms removed, and O<sub>br</sub>-all for the surface with no O<sub>br</sub> atoms (Figure 2d). The other stable surfaces are O<sub>s</sub>-half with every other

**Table 1. Calculated Vertical Layer Spacings,  $d$  (Å), and Percent Relaxations with Respect to Theoretical Bulk Spacings for Selected Stable Surface Terminations of the  $\beta$ -MnO<sub>2</sub> (110) Surface<sup>a</sup>**

layers	stoichiometric		O <sub>s</sub> -half		O <sub>s</sub> -all		O <sub>s</sub> -half/O <sub>br</sub> -all	
	$d$	% $\Delta$	$d$	% $\Delta$	$d$	% $\Delta$	$d$	% $\Delta$
1–2	1.130	–8	0.816	–34	0.085	–93		
2–3 Mn5	1.121	–9	1.234	0	–0.586	–148	0.540	–56
Mn6	1.315	+7	0.921	–25	–0.116	–109	0.092	–93
O <sub>s</sub>	1.378	+12	1.796	+46			1.243	+1
3–4	0.669	–3	0.607	–12	2.452	+257	0.956	+39
4–5	1.274	+3	1.294	+5	1.248	+1	1.354	+10
5–6 Mn5	1.199	–3	1.210	–2	1.253	+2	1.183	–4
Mn6	1.269	+3	1.195	–3	1.120	–9	1.297	+5
O <sub>s</sub>	1.235	0	1.103	–11	1.430	+16	1.397	+13
			(1.404)	(+14)			(1.471)	(+19)

<sup>a</sup>Numbers in parentheses are for atoms below the O<sub>s</sub> vacancy at the surface.

**Table 2. Calculated Lateral Relaxations (Å) with Respect to Theoretical Bulk Positions for Selected Stable Surface Terminations of the  $\beta$ -MnO<sub>2</sub> (110) Surface<sup>a</sup>**

layers	stoichiometric	O <sub>s</sub> -half	O <sub>s</sub> -all	O <sub>s</sub> -half/O <sub>br</sub> -all
	[1 $\bar{1}$ 0]	[1 $\bar{1}$ 0]	[1 $\bar{1}$ 0]	[1 $\bar{1}$ 0]
1	+0.01	–1.51	–1.24	
2 Mn5	+0.01	–0.23	+0.04	+1.44
Mn6	+0.01	–0.51	+0.05	+1.70
O <sub>s</sub>	–0.02, +0.05	+0.03		+1.69
3	+0.01	+0.33	+1.33	+0.18
4	0	+0.06	0	–0.05
5 Mn5	+0.01	+0.12	–0.01	+0.08
Mn6	+0.01	+0.15	–0.01	+0.03
O <sub>s</sub>	0, +0.02	+0.14 (+0.13)	±0.02	+0.05 (+0.03)
6	+0.01	+0.20	–0.01	+0.08
7	0	–0.06	+0.01	0

<sup>a</sup>Numbers in parentheses are for atoms below the O<sub>s</sub> vacancy at the surface.

row of O<sub>s</sub> atoms removed (Figure 2e), O<sub>s</sub>-all with all O<sub>s</sub> atoms removed (Figure 2f), and O<sub>s</sub>-half/O<sub>br</sub>-all with every other row of O<sub>s</sub> atoms and all O<sub>br</sub> atoms removed from the surface (Figure 2g). Surfaces with other O<sub>s</sub> vacancies were also studied, but none of them are stable within the range of accessible  $\mu_{\text{O}}$ .

The stoichiometric surface is the most stable at thermodynamic equilibrium over a large portion of the range of  $\mu_{\text{O}}$  values with  $\gamma = 52.1 \text{ meV}/\text{Å}^2$  (Figure 3). This result is consistent with the experimental determination of an average manganese valence of 4.0 at the surface of  $\beta$ -MnO<sub>2</sub>,<sup>26</sup> which is not observed for the oxidized and reduced surfaces (see discussion below). Above a  $\mu_{\text{O}}$  value of  $-0.17 \text{ eV}$ , oxygen can be added to the surface to form an as yet unreported manganyl (Mn=O) group, as demonstrated by the stability of the manganyl surface in this regime. The  $\mu_{\text{O}}$  value at the crossover between the stoichiometric and manganyl

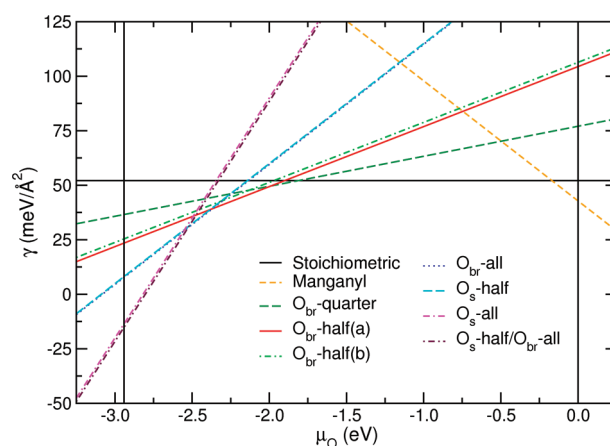


**Figure 3.** Surface free energies of various surface terminations of the  $\beta$ -MnO<sub>2</sub> (110) surface as determined by ab initio thermodynamics as a function of  $\mu_{\text{O}}$  at 0 K. The vertical black lines bracket the range of accessible  $\mu_{\text{O}}$  values as defined in the text.

surfaces corresponds to an ambient oxygen partial pressure  $p_{\text{O}_2}$  of 0.2 bar and a temperature of 193 K, and higher pressures and lower temperatures (more oxidizing conditions) should lead to formation of the manganyl surface reconstruction. As  $\mu_{\text{O}}$  decreases below  $-1.81 \text{ eV}$  (at UHV conditions of  $p_{\text{O}_2} = 10^{-10} \text{ bar}$ ,  $T = 876 \text{ K}$ ), O<sub>br</sub> vacancies are formed on the surface, with O<sub>br</sub>-quarter becoming more stable than the stoichiometric surface. The O<sub>br</sub>-half(a) and O<sub>br</sub>-half(b) surfaces differ in  $\gamma$  by only  $1.9 \text{ meV}/\text{Å}^2$  and are the most stable surfaces between  $-1.99$  and  $-2.37 \text{ eV}$ . This range of  $\mu_{\text{O}}$  values translates to a temperature range of 960–1140 K at a  $p_{\text{O}_2}$  of  $10^{-10} \text{ bar}$ . Then the O<sub>br</sub>-all surface becomes lowest in  $\gamma$  over a small range of  $\mu_{\text{O}}$  ( $0.16 \text{ eV}$ ). This surface is essentially degenerate with O<sub>s</sub>-half with only a  $0.40 \text{ meV}/\text{Å}^2$  separation in  $\gamma$ . Below a  $\mu_{\text{O}}$  of  $-2.53 \text{ eV}$  ( $1210 \text{ K}$  at  $10^{-10} \text{ bar}$ ), the fully reduced O<sub>s</sub>-all and O<sub>s</sub>-half/O<sub>br</sub>-all surfaces are most stable. The O<sub>s</sub>-all surface is  $1.6 \text{ meV}/\text{Å}^2$  higher in  $\gamma$  than O<sub>s</sub>-half/O<sub>br</sub>-all.

Interestingly, enthalpic and entropic contributions to  $\gamma$  at finite temperatures lead to a different ordering of the most stable surfaces. At 298.15 K, these contributions lower  $\gamma$  by  $16 \text{ meV}/\text{Å}^2$  to  $23 \text{ meV}/\text{Å}^2$ , and they become significantly larger at higher temperatures (e.g.,  $-73 \text{ meV}/\text{Å}^2$  to  $-95 \text{ meV}/\text{Å}^2$  at 600 K). These results illustrate the importance of considering entropic contributions to metal oxide surfaces, even in the absence of hydroxylated species. For example, reduction of the surface is predicted to proceed via O<sub>br</sub>-half(b), O<sub>br</sub>-all, and O<sub>s</sub>-half/O<sub>br</sub>-all at finite temperature, and O<sub>br</sub>-quarter and O<sub>br</sub>-half(a) are no longer predicted to be observed. Generally, inclusion of the entropic contributions to  $\gamma$  shifts the oxidation temperature to a lower value at a given  $p_{\text{O}_2}$ , and reduction temperatures are shifted to higher values than those specified by  $\mu_{\text{O}}$  alone. Detailed discussion of the oxidation and reduction temperature thresholds at ambient and UHV  $p_{\text{O}_2}$  (0.2 bar and  $10^{-10} \text{ bar}$ , respectively) is given in the Supporting Information. Here, we point out that the temperature at which reduction begins (forming O<sub>br</sub>-half(b)) is predicted to be 1030 K under UHV conditions. This calculated decomposition temperature is higher than the known decomposition temperature of MnO<sub>2</sub> of 808 K<sup>69</sup> because decomposition probably begins at lower oxygen vacancy concentrations than studied here. The results presented here provide an upper limit for the decomposition temperature when a significant

fraction of oxygen atoms are simultaneously removed from the surface. Because the decomposition temperature depends on kinetic factors, which are not included in our model, and the decomposition mechanism is unknown, comparison between the calculated and experimental decomposition temperatures should be made with caution.

**B. Oxidized and Reduced Surface Reconstructions.** Prior to this study, it was unclear which surface structures may exist under different temperature and pressure regimes and what redox behavior the surface may exhibit in response to variations in  $\mu_{\text{O}}$ . By examining a number of oxidized and reduced surfaces, it was found that the  $\beta\text{-MnO}_2$  (110) stoichiometric surface is the only relevant surface at conditions typical in most experimental settings. Yet, the surface reconstructions studied in this work may provide insight into the role of manganese at the atomic level in redox reactions important in the environment and in technological applications. For example, sensors are often employed at high temperatures where redox chemistry occurs. Although we have investigated only oxygen partial pressure and temperature dependence, other reducing conditions are possible as well, such as the presence of heavy metal ions or organic matter that can stimulate redox chemistry. Here, we discuss the interesting relationship between manganese oxidation state, coordination geometry, and d-orbital energy exhibited by the (110) surface, which is an important driver in the surface reconstructions and has implications for the redox behavior of manganese.

Oxidation of the surface occurs by addition of oxygen to complete the coordination sphere of Mn5 under oxygen-rich, low-temperature conditions (above  $\mu_{\text{O}} = -0.17$ , corresponding to a temperature of 193 K at  $p_{\text{O}_2} = 0.2$  bar). As shown in Figure 2c, the additional oxygen atoms pull Mn5 atoms out of the surface, and manganyl groups ( $\text{Mn}=\text{O}$ ) form at the manganyl surface. These structural transformations lead to an increase in the Mn5-layer 4 oxygen bond length from 1.92 Å in the bulk to 2.40 Å and to an O–Mn5 bond distance of 1.55 Å at the surface. The short O–Mn5 bond length is comparable to the 1.59 Å  $\text{Fe}=\text{O}$  bond length calculated for the ferryl-terminated  $\alpha\text{-Fe}_2\text{O}_3$  (0001) surface.<sup>78</sup> The vertical and lateral relaxations for the manganyl surface are given in the Supporting Information. The oxidation of Mn5 leads to pairing of all d electrons, as demonstrated by calculated Mulliken and Hirshfeld spins of 0.00. These spin values suggest that Mn5 is oxidized to no-spin  $\text{Mn}^{\text{V}}$ . Additional electron density is pulled from other surface and subsurface atoms, particularly  $\text{O}_{\text{br}}$  and layer 5 manganese under Mn5, as determined by changes in spin upon oxidation of the surface. A comparison of the partial density of states of Mn5 on the stoichiometric and manganyl surfaces shows the increase in energy of the d orbitals due to electron pairing on the manganyl surface (details given in the Supporting Information).

Reduction of the surface in the intermediate range of  $\mu_{\text{O}}$  favors removal of bridging oxygen ( $\text{O}_{\text{br}}$ ) atoms. At 0 K, the percent of  $\text{O}_{\text{br}}$  vacancies increases with decreasing  $\mu_{\text{O}}$ , proceeding through  $\text{O}_{\text{br}}$ -quarter;  $\text{O}_{\text{br}}$ -half(a); and  $\text{O}_{\text{br}}$ -half(b); and finally,  $\text{O}_{\text{br}}$ -all (Figure 2d). Generally, buckling of the surface in which the  $\text{O}_{\text{s}}$  atoms relax out of the surface occurs for all surfaces with  $\text{O}_{\text{br}}$  vacancies, and this buckling is most evident for the  $\text{O}_{\text{br}}$ -all surface (see Figure 2d). Surface relaxations for these surfaces are listed in the Supporting Information.  $\text{O}_{\text{br}}$  vacancies leave 5-fold coordinated Mn6 on the  $\text{O}_{\text{br}}$ -quarter and  $\text{O}_{\text{br}}$ -half(a) surfaces and 4-fold coordinated Mn6 on the  $\text{O}_{\text{br}}$ -half(b) and  $\text{O}_{\text{br}}$ -all surfaces. Generally, additional electrons acquired at the surface by removal of neutral  $\text{O}_{\text{br}}$  atoms localize to surface manganese atoms with

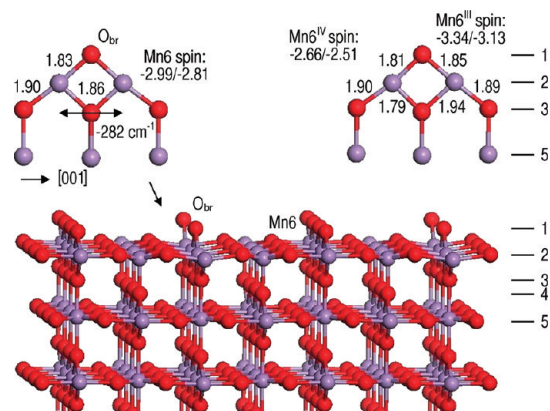


**Figure 4.** Illustration of the imaginary frequency found for the  $\beta\text{-MnO}_2$  (110)  $\text{O}_{\text{br}}$ -quarter surface when 5-fold coordinated Mn6 are equivalent (left) and of the symmetry-broken geometry of Mn6 (right). Bond lengths are in angstroms. The first spin value is the Mulliken spin, and the second value is the Hirshfeld spin. The slab of the symmetric surface is viewed along the [001] direction. (O, red/dark sphere; Mn, purple/light sphere).

unfilled coordination shells, reducing them to high-spin  $\text{Mn}^{\text{III}}$  and demonstrating the stability of octahedral  $\text{Mn}^{\text{IV}}$ . The number of reduced manganese atoms at the surface increases with the percent of  $\text{O}_{\text{br}}$  vacancies, and at or above vacancy concentrations of 50%, Mn5 is also reduced. Only the  $\text{O}_{\text{br}}$ -quarter and  $\text{O}_{\text{br}}$ -all surfaces exhibit some delocalization of the additional electron density over other surface and subsurface atoms, as shown by changes in their spins upon surface reduction.

Interestingly, highly symmetric surfaces are found to be metastable in some cases, and Jahn–Teller distortion of surface manganese is necessary to break the symmetry and locate a true minimum-energy structure. The reduced symmetry at the surface allows electrons to localize to one surface manganese instead of being shared by adjacent manganese atoms. For example, adjacent 5-fold coordinated Mn6 atoms on the  $\text{O}_{\text{br}}$ -quarter surface initially share an electron, as indicated by an average increase in the magnitude of their Mulliken and Hirshfeld spins by 0.47 relative to the stoichiometric surface. This partial reduction of Mn6 is revealed to be a metastable state by vibrational analysis, which shows a doubly degenerate imaginary frequency at  $-282\text{ cm}^{-1}$ . This frequency is associated with the layer 3 oxygen under  $\text{O}_{\text{br}}$  attached to 5-fold coordinated Mn6 translating along the [001] direction (Figure 4). Perturbing this layer 3 oxygen along the [001] direction breaks the degeneracy of the two neighboring 5-fold coordinated Mn6 atoms, leading to the location of a true minimum-energy surface. Adjacent 5-fold coordinated Mn6 lose their electronic and structural equivalency as the shared electron becomes localized on one Mn6, resulting in high-spin  $\text{Mn}^{\text{III}}$  and  $\text{Mn}^{\text{IV}}$  on the surface (see Figure 4).

The  $\text{O}_{\text{br}}$ -half(a) surface also initially optimizes to a symmetric metastable state with an electron delocalized between two 5-fold coordinated Mn6. Vibrational analysis identifies large imaginary frequencies at  $-276$  and  $-317\text{ cm}^{-1}$  for this surface. As in the earlier case, symmetry is broken by distorting the structure along the dominant imaginary mode, and a lower-energy true minimum is found with the shared electron localized to one of the 5-fold coordinated Mn6. The effect of electronically and structurally inequivalent Mn6 at the surface leads to variations in surface relaxations for the Mn6 atoms and their neighbors, which are shown in the Supporting Information.

As  $\mu_{\text{O}}$  approaches the lower limit of accessible  $\mu_{\text{O}}$  values, surfaces missing every other row of  $\text{O}_{\text{s}}$  atoms or all  $\text{O}_{\text{s}}$  atoms are thermodynamically stable (Figure 3). Although it is not known if these surfaces would be observed outside of the UHV environment, they exhibit surface reconstructions significantly different from those observed for other rutile-type metal oxides and hence are discussed in detail. Because of the significant reconstructions, thicker surface slabs were tested to ensure proper convergence of the  $\text{O}_{\text{s}}$ -half and  $\text{O}_{\text{s}}$ -half/ $\text{O}_{\text{br}}$ -all geometries and  $\gamma$ . For  $\text{O}_{\text{s}}$ -half,  $\gamma$  is converged within  $0.17 \text{ meV}/\text{\AA}^2$  with five metal layers, and vertical surface relaxations vary no more than  $\pm 1\%$  compared with a seven-metal-layer slab. The  $\text{O}_{\text{s}}$ -half/ $\text{O}_{\text{br}}$ -all surface requires the use of six metal layers to achieve convergence of  $\gamma$  within  $0.11 \text{ meV}/\text{\AA}^2$  and differences in vertical surface relaxations between  $\pm 1\%$  for the first four layers.

Prior to relaxation, the  $\text{O}_{\text{s}}$ -half surface consists of 3-fold coordinated Mn5 in a geometry resembling half of an octahedron and square pyramidal Mn6 (see Figure 1). Relaxation results in the formation of tetrahedral Mn5 and square planar Mn6 as Mn6 and  $\text{O}_{\text{br}}$  fall toward Mn5 (see Figures 1 and 2e). Both Mn5 and Mn6 adopt high-spin  $\text{Mn}^{\text{III}}$  electronic configurations, as demonstrated by Mulliken spins of 3.30 and  $-3.69$ , respectively. The reduction of surface manganese plays a role in the large translations of surface atoms (see discussion below in the Molecular Orbital Analysis section), which lead to significant vertical and lateral relaxations (Tables 1 and 2, respectively). Although Mn5 experiences no vertical relaxation,  $\text{O}_{\text{br}}$ , Mn6, and layer 3 oxygen atoms relax into the surface by  $-34\%$ ,  $-25\%$ , and  $-12\%$ , respectively, relative to the bulk. The row of  $\text{O}_{\text{s}}$  atoms remaining on the surface undergoes expansion by  $+46\%$ . The formation of square planar Mn6 occurs by lateral translations of  $-1.51 \text{ \AA}$  and  $-0.51 \text{ \AA}$  of  $\text{O}_{\text{br}}$  and Mn6, respectively, along the  $[1\bar{1}0]$  direction and by movement of layer 3 oxygen atoms  $+0.33 \text{ \AA}$  in the opposite direction. Mn5 atoms also relax  $-0.23 \text{ \AA}$  in the  $[1\bar{1}0]$  direction. Generally, the large negative translations of  $\text{O}_{\text{br}}$ , Mn6, and Mn5 are compensated by positive translations along the  $[1\bar{1}0]$  direction in the subsurface layers (Table 2).

The  $\text{O}_{\text{s}}$ -all surface initially optimizes to a reconstruction similar to the stoichiometric one without  $\text{O}_{\text{s}}$  (Mn5 is coordinated only to layer 4 oxygen, and Mn6 is square planar). This surface reconstruction is metastable as vibrational analysis reveals four large imaginary frequencies associated with wagging of square planar Mn6 along the  $[1\bar{1}0]$  direction (toward Mn5). After perturbation along the dominant imaginary mode, a new structure that is  $122 \text{ meV}/\text{\AA}^2$  lower in  $\gamma$  is found. The reconstruction proceeds by square planar Mn6 rotating  $90^\circ$  around  $[001]$  so that  $\text{O}_{\text{br}}$  and layer 3 oxygen atoms end up in the approximate plane of layer 2, and it appears to be the result of  $\text{O}_{\text{br}}$  and subsurface oxygen removal (see Figure 2f). Trigonal planar Mn5 is formed at the surface. Mn5, Mn6, and layer 5 square pyramidal manganese are calculated to have Mulliken spins of 3.94,  $-3.68$ , and 3.21, respectively, signifying reduction to high-spin  $\text{Mn}^{\text{III}}$ . Additional electron density is delocalized among  $\text{O}_{\text{br}}$  and subsurface atoms, as demonstrated by changes in their spins. This surface reconstruction is a metastable state with perturbations along the imaginary mode leading to the same structure. Large vertical relaxations relative to the bulk are associated with this reconstruction (Table 1).  $\text{O}_{\text{br}}$ , Mn5, and Mn6 experience significant relaxations of  $-93\%$ ,  $-148\%$ , and  $-109\%$ , respectively, into the surface, whereas layer 3 oxygen atoms relax out of the surface by  $+257\%$ . If the reconstruction is considered to result from removal of  $\text{O}_{\text{br}}$  and layer 3 oxygen (if they are treated as  $\text{O}_{\text{s}}$  atoms), then

the calculated relaxations measured relative to layer 4 oxygen are more modest, with relaxations of  $-3\%$ ,  $+22\%$ , and  $+27\%$  for Mn5, Mn6, and  $\text{O}_{\text{s}}$ , respectively (not shown in table). Rotation of square planar Mn6 causes considerable lateral relaxation of  $\text{O}_{\text{br}}$  by  $-1.24 \text{ \AA}$  and of layer 3 oxygen by  $+1.33 \text{ \AA}$  along the  $[1\bar{1}0]$  direction. Layer 5 oxygen atoms move  $0.02 \text{ \AA}$  away from the square pyramidal layer 5 manganese (Table 2; see Figure 2f).

In contrast to  $\text{O}_{\text{s}}$ -all, the  $\text{O}_{\text{s}}$ -half/ $\text{O}_{\text{br}}$ -all reconstruction shown in Figure 2g looks significantly different from the stoichiometric one. Prior to relaxation, the  $\text{O}_{\text{s}}$ -half/ $\text{O}_{\text{br}}$ -all surface contains 3-fold coordinated Mn5 and Mn6 with half-octahedral geometries. Relaxation of the surface leads to the formation of distorted Mn5 tetrahedra in which three of the oxygen atoms (two  $\text{O}_{\text{s}}$  atoms and a layer 3 oxygen) are nearly planar with Mn5 (Figure 2g). Mn6 assumes a distorted octahedral geometry completed by two  $\text{O}_{\text{s}}$ , one layer 3 oxygen, two layer 4 oxygen, and a layer 6 oxygen. Layer 3 oxygen atoms become 4-fold coordinated, and layer 4 oxygen atoms are 5-fold coordinated. The reduced surface manganese atoms are calculated to have Mulliken spins of 3.91 on Mn5 and  $-4.56$  on Mn6, indicative of high-spin  $\text{Mn}^{\text{III}}$  and high-spin  $\text{Mn}^{\text{II}}$ , respectively. The fourth electron added to the surface by removal of neutral oxygen atoms is delocalized among the subsurface manganese atoms. This reconstruction is accompanied by significant vertical relaxations (Table 1). Surface manganese atoms experience large relaxations of  $-56\%$  for Mn5 and  $-93\%$  for Mn6 into the surface. The layer 2 atoms move approximately a quarter of the unit cell length in the  $[1\bar{1}0]$  direction, leading to a surface reconstruction in which the first layer of metal atoms is displaced at least  $1.44 \text{ \AA}$  along the  $[1\bar{1}0]$  direction relative to the bulk (Table 2). This surface reconstruction is significantly different from the  $\text{O}_{\text{s}}$ -half/ $\text{O}_{\text{br}}$ -all surface of rutile-type  $\text{SnO}_2$ , which was found to be the most stable reduced surface in GGA studies.<sup>35,63</sup> For  $\text{SnO}_2$ , the relaxations are similar to the stoichiometric surface. The difference in the relaxations between these two rutile-type structures is most likely a factor of the difference in d-orbital filling, with full d orbitals on tin and partially filled d orbitals on manganese.

*C. Molecular Orbital Analysis.* To understand the driving force for the surface reconstructions, the relationship between oxidation state, coordination geometry, and d-orbital energy levels was investigated. When the surface is reduced, the extra electrons at the surface can cause surface reconstruction in which surface manganese atoms adopt new coordination geometries with more energetically favorable d-orbital occupations. The d-orbital populations and energies were calculated for the surface manganese before and after surface relaxation using representative molecular complexes to elucidate the role of the d orbitals in directing surface reconstruction. The following procedure was used. Molecular complexes of surface manganese atoms were obtained by cutting a manganese atom with its coordinated oxygen atoms from the unrelaxed and relaxed surfaces (see Figure 1). The oxygen atoms were saturated with hydrogen atoms to form  $\text{Mn}(\text{H}_2\text{O})_x$  complexes, and only the positions of the hydrogen atoms were optimized for various manganese oxidation states. The same level of theory and basis set were used in these nonperiodic calculations as were employed in the periodic calculations detailed previously, but the cutoff radius was increased to  $5.5 \text{ \AA}$  to obtain accurate energies. The eigenvalues of the d orbitals were then calculated. The d-band center, or average d-orbital energy, shifts with coordination number and geometry. To understand how d-orbital splitting and occupations stabilize or destabilize molecular complexes with different coordination

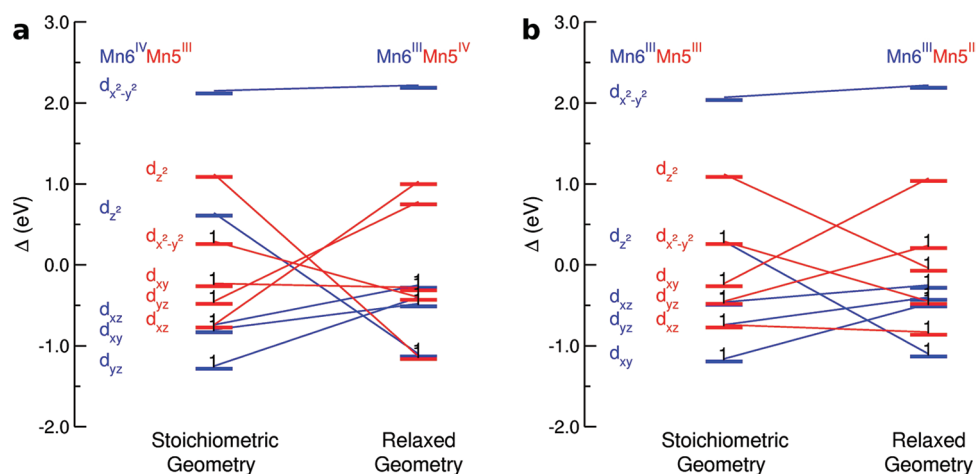


**Figure 5.** The difference in energies between the spin-up d orbitals and their average ( $\Delta$ ) for Mn5 and Mn6 on the  $\beta$ - $\text{MnO}_2$  (110)  $\text{O}_s$ -half surface. (a) Mn5 starts as  $\text{Mn}^{\text{III}}$ , Mn6 starts as  $\text{Mn}^{\text{IV}}$ , and they switch oxidation states. (b) Mn5 and Mn6 maintain the 3+ oxidation state during relaxation.

numbers, the center of the majority d “band” (average spin-up d-orbital energies) was determined, and the difference between the d orbital of interest and the “band” center ( $\Delta$ ) was used.

First, a discussion of fully relaxed molecular  $\text{Mn}(\text{H}_2\text{O})_x$  complexes is warranted. For  $\text{Mn}^{\text{IV}}$  complexes, only low-spin tetrahedral and high-spin trigonal bipyramidal, square pyramidal, and octahedral geometries were found.  $\text{Mn}^{\text{IV}}$  is observed in tetrahedral and octahedral geometries in nature.<sup>79</sup> Summing the  $\Delta$  values of the filled d orbitals gives the following sequence for stability: tetrahedral ( $-3.49$  eV) > octahedral ( $-3.00$  eV) > square pyramidal ( $-2.53$  eV) > trigonal bipyramidal ( $-2.51$  eV). Note that the total energy of the trigonal bipyramidal  $\text{Mn}^{\text{IV}}$  complex was found to be 0.68 eV higher than that of the square pyramid, demonstrating that these relative stabilities are reliable.

$\text{Mn}^{\text{III}}$  complexes exhibit larger diversity in possible coordination geometries. In nature,  $\text{Mn}^{\text{III}}$  can be found in trigonal planar, square planar, trigonal bipyramidal, square pyramidal, and octahedral geometries.<sup>79</sup> Stable, high-spin  $\text{Mn}^{\text{III}}$  complexes in each of these geometries were found, although the trigonal bipyramidal complex optimized to a square pyramidal complex when the force tolerance was lower than 0.05 eV/Å. Generally, a force tolerance of 0.01 eV/Å does not significantly change the energies of the d orbitals, and the trigonal bipyramidal results obtained with a 0.05 eV/Å force tolerance will be used in the following discussion.  $\text{Mn}^{\text{III}}$  tetrahedra relax to square planar complexes in the absence of symmetry constraints and will not be discussed further. The square planar complex is the most stable, on the basis of the sum of the  $\Delta$  values of the filled d orbitals ( $-2.02$  eV). The rest of the complexes can be ranked in terms of stability as follows: square pyramidal ( $-1.47$  eV) > trigonal planar ( $-1.45$  eV) > trigonal bipyramidal ( $-1.31$  eV) > octahedral ( $-1.24$  eV). The square pyramidal complex is calculated to be 0.47 eV lower in total energy than the trigonal bipyramidal complex, in qualitative agreement with these results.

The relative energies of the  $\text{Mn}^{\text{III}}$  molecular complexes indicate that the square planar geometry affords the lowest-energy orbital occupancies for the four d electrons. This favorable arrangement of d electrons thus likely constitutes the predominant driving force for the  $\text{O}_s$ -half surface reconstruction (Figure 2e), since Mn6 relaxes from a square pyramid to a square planar coordination geometry (see Figure 1). The assignment of Mn5 and Mn6 oxidation states is more complicated than initially

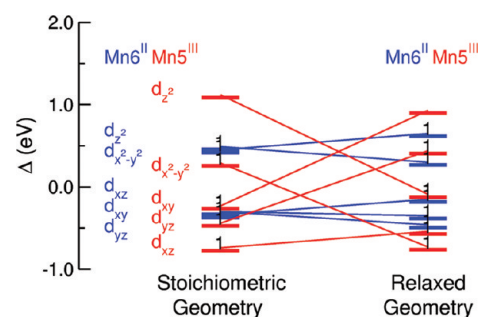


**Figure 6.** The difference in energies between the spin-up d orbitals and their average ( $\Delta$ ) for Mn5 and Mn6 on the  $\beta$ - $\text{MnO}_2$  (110)  $\text{O}_s$ -half/ $\text{O}_{\text{br}}$ -all surface.

stated, as demonstrated by a comparison of Mn5 and Mn6 spins before and after relaxation to the spins on analogous  $\text{Mn}(\text{H}_2\text{O})_x$  molecular complexes with formal 3+ or 4+ oxidation states (see Figure 1). Prior to relaxation, Mn5 has a 3+ oxidation state, and Mn6 falls between  $\text{Mn}^{\text{III}}$  and  $\text{Mn}^{\text{IV}}$ . Relaxation leads to transfer of some electron density from Mn5 to Mn6 so that Mn5 is now between  $\text{Mn}^{\text{III}}$  and  $\text{Mn}^{\text{IV}}$  and Mn6 is  $\text{Mn}^{\text{III}}$ . These results indicate two possibilities: electron transfer between Mn5 and Mn6 leads to a switching of oxidation states upon relaxation, or both Mn5 and Mn6 maintain 3+ oxidation states during relaxation. The  $\Delta$  values for the Mn5 and Mn6 spin-up d orbitals are shown for both cases in Figure 5. Both scenarios are accompanied by a decrease in the sum of filled d-orbital  $\Delta$  values of  $\sim 0.1$  eV. If electron transfer occurs from Mn5 to Mn6 (Figure 5a), then Mn5 and Mn6 relax to the most stable coordination geometries for  $\text{Mn}^{\text{IV}}$  and  $\text{Mn}^{\text{III}}$  determined by examining fully relaxed  $\text{Mn}(\text{H}_2\text{O})_x$  complexes. Transfer of electrons from the  $d_{xz}$  and  $d_{yz}$  orbitals on Mn5 to the  $d_{z^2}$  orbitals on Mn5 and Mn6 results in a large decrease in the sum of their  $\Delta$  values by 1.0 eV. The Mn5  $d_{x^2-y^2}$  orbital also falls by 0.69 eV in energy. Most of the decrease in d-orbital energy is counteracted by increased  $\Delta$  values for the rest of the filled d orbitals on Mn6, explaining the small overall decrease in d-orbital energies. The second scenario shows similar changes in relative  $\Delta$  values (Figure 5b), although the driving force in this case is the decrease in the Mn6  $d_{z^2}$   $\Delta$  value upon transformation to a square planar geometry. The real picture is probably a combination of the two scenarios and illustrates the

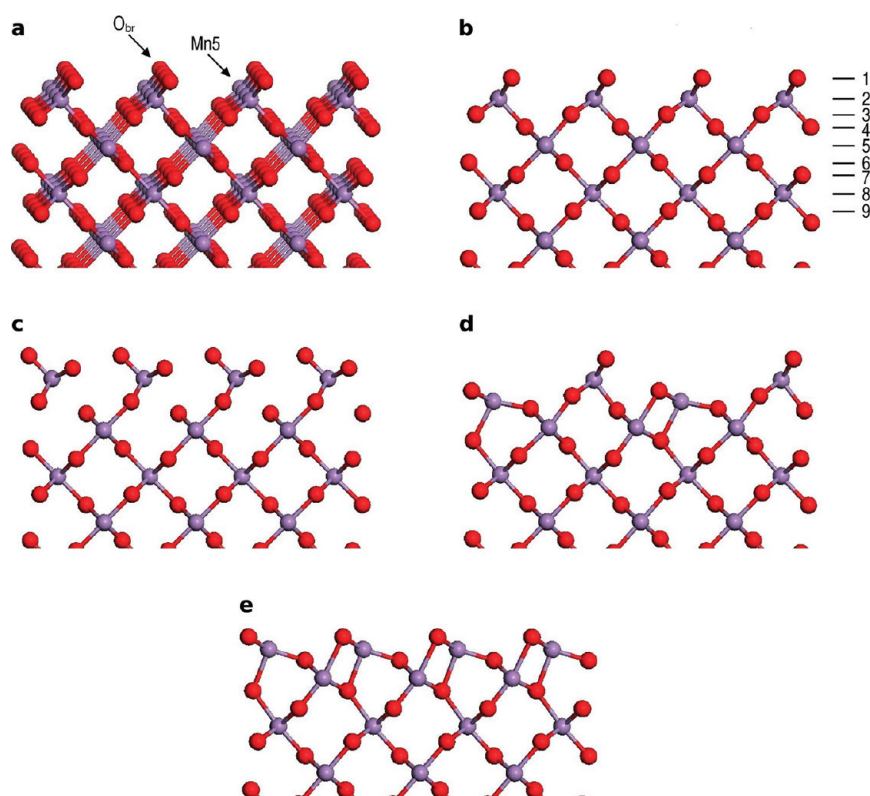


**Figure 7.** (a)  $\beta$ - $\text{MnO}_2$  (100) stoichiometric surface showing surface atom types; stable (100) surface terminations viewed along the [001] direction: (b) stoichiometric showing layer stacking sequence; (c) manganyl; (d)  $\text{O}_{\text{br}}\text{-half}$ (b); (e)  $\text{O}_{\text{br}}\text{-all}$  (O, red/dark sphere; Mn, purple/light sphere).

importance of lowering the  $d_{z^2}$  orbital energy on stabilizing square planar  $\text{Mn}^{\text{III}}$  at the surface. Although other electrostatic and steric interactions may affect the surface reconstruction, it is likely that the formation of square planar  $\text{Mn}^{\text{III}}$  accounts for a significant portion of the predicted stability of  $\text{O}_{\text{s}}\text{-half}$  at low  $p_{\text{O}_2}$  and high temperature.

The other surface displaying significant reconstruction during relaxation is the  $\text{O}_{\text{s}}\text{-half}/\text{O}_{\text{br}}\text{-all}$  surface (Figure 2g). As discussed previously, Mn5 and Mn6 are initially 3-fold coordinated, half-octahedral species. Mn5 relaxes to a distorted tetrahedron, and Mn6 optimizes to a significantly distorted octahedron. Mn5 and Mn6 maintain the same oxidation states ( $\text{Mn}^{\text{III}}$  and  $\text{Mn}^{\text{II}}$ , respectively) during relaxation. Figure 6 shows the  $\Delta$  values for Mn5 and Mn6 before and after optimization. For this surface, formation of the distorted octahedron causes splitting of the  $e_{\text{g}}$  and  $t_{2\text{g}}$  orbitals on Mn6. The distorted tetrahedral Mn5 should not be stable, given the 3+ oxidation state, and an increase in the sum of the filled d-orbital  $\Delta$  values is observed. Hence, in this case, the lowering of the d-orbital energies is not sufficient to explain the surface reconstruction. The driving force for the reconstruction instead appears to be related to the competition between dissatisfied  $\text{Mn}^{\text{II}}$  and  $\text{Mn}^{\text{III}}$  in 3-fold coordinated, half-octahedral geometries and steric and electrostatic constraints of the slab. When complexes representing 3-fold coordinated, half-octahedral  $\text{Mn}^{\text{II}}$  and  $\text{Mn}^{\text{III}}$  are fully relaxed, the final structure is trigonal planar. In agreement with these results, the reconstruction of the surface proceeds as Mn6 falls into the surface to become trigonal planar, which also results in approximately trigonal planar Mn5. At this point, the rows of Mn5 and Mn6 at the surface are separated by only 2.12 Å along the  $[1\bar{1}0]$  direction, with a Mn5–Mn6 distance of 2.56 Å. Mn5 moves away

from Mn6 along the  $[1\bar{1}0]$  direction and coordinates to a layer 3 oxygen atom, resulting in a nearly trigonal planar geometry with a fourth oxygen ligand (layer 4 oxygen) at a distance of 2.11 Å. Mn6 moves along the surface with Mn5 to prevent reformation of 3-fold coordinated, half-octahedral Mn6. This translation results in bond formation between Mn6 and three oxygen atoms, two in layer 4 and one in layer 6. This surface reconstruction demonstrates the interplay between relaxation to geometries with lower d-orbital energies, steric constraints of the subsurface layers, and electrostatic interactions, which lead to new and as yet unobserved surface reconstructions. In this case, energy gains from new steric and electrostatic interactions appear to be greater than those from electronic differences.

These case studies can provide insight into the stability of the  $\text{O}_{\text{s}}\text{-all}$  surface reconstruction and why other surfaces with a fraction of  $\text{O}_{\text{s}}$  atoms removed are not found to be stable in the range of accessible  $\mu_{\text{O}}$ . Before perturbation of square planar Mn6 toward Mn5, the  $\text{O}_{\text{s}}\text{-all}$  surface is metastable because Mn5 has only one oxygen ligand and is unsatisfied. Breaking the symmetry of the metastable state allows reconstruction to a favorable trigonal planar  $\text{Mn}^{\text{III}}$  while also maintaining the stable square planar  $\text{Mn}^{\text{III}}$ . As demonstrated by the calculations on fully relaxed  $\text{Mn}^{\text{III}}(\text{H}_2\text{O})_x$  molecular complexes, the relatively low energies of the filled d orbitals for these two coordination geometries is likely the driving force for the  $\text{O}_{\text{s}}\text{-all}$  reconstruction. If only a fraction of  $\text{O}_{\text{s}}$  atoms are removed from the surface, 3- or 4-fold coordinated Mn5 atoms in octahedral-like geometries typically remain at the surface. These  $\text{Mn}^{\text{III}}$  species would prefer to be trigonal planar or square planar; however, the steric constraints of the surface and subsurface layers prevent relaxation into the surface to form these geometries. In some cases,

**Table 3. Calculated Vertical Layer Spacings,  $d$  (Å), and Percent Relaxations with Respect to Theoretical Bulk Spacings for Selected Stable Surface Terminations of the  $\beta$ -MnO<sub>2</sub> (100) Surface**

layers	stoichiometric		O <sub>br</sub> -all	
	$d$	% $\Delta$	$d$	% $\Delta$
1–2	0.969	+11		
2–3	0.735	–16	–0.583	–167
3–4	0.591	+22	1.105	+127
4–5	0.843	–3	0.839	–4
5–6	0.827	–5	0.601	–31
6–7	0.567	+17	0.827	+70
7–8	0.849	–3	0.841	–3
8–9	0.840	–4	0.728	–16

**Table 4. Calculated Lateral Relaxations (Å) with Respect to Theoretical Bulk Positions for Selected Stable Surface Terminations of the  $\beta$ -MnO<sub>2</sub> (100) Surface**

layers	stoichiometric	O <sub>br</sub> -all
	[010]	[010]
1	–0.21	
2	+0.07	–0.45
3	–0.13	–0.53
4	–0.06	–0.10
5	+0.02	–0.12
6	+0.03	+0.17
7	+0.02	+0.10
8	+0.01	+0.02
9	–0.03	–0.10
10	–0.02	–0.08

metastable states were found initially for surfaces with a fraction of O<sub>s</sub> atoms removed, and location of the true minima resulted in significantly lower  $\gamma$  values. Yet, these surfaces are not stable in the accessible range of  $\mu_{\text{O}}$  values. One such example is the surface with alternating O<sub>s</sub> vacancies along the [001] and [110] directions (50% O<sub>s</sub> vacancies). This surface is only 16.8 meV/Å<sup>2</sup> higher in  $\gamma$  than the O<sub>br</sub>-all surface at 0 K and has an interesting surface reconstruction with tetrahedral MnS<sup>IV</sup> and distorted square planar, trigonal bipyramidal, and square pyramidal Mn<sup>III</sup>. The surface manganese are essentially inaccessible to adsorbate molecules. Generally, for reduction of the surface to occur by O<sub>s</sub> atom removal, enough O<sub>s</sub> atoms need to be removed to allow for significant surface reconstruction to more favorable Mn<sup>III</sup> geometries.

**2. (100) Surface.** On the stoichiometric  $\beta$ -MnO<sub>2</sub> (100) surface, 5-fold coordinated manganese atoms (Mn5) are connected by rows of bridging oxygen atoms (O<sub>br</sub>) along the [001] direction (Figure 7a). Mn5 maintains a high-spin Mn<sup>IV</sup> oxidation state with calculated Mulliken and Hirshfeld spins of –2.63 and –2.47, respectively, comparable to the bulk Mn<sup>IV</sup> values of 2.59 and 2.40. Unlike the (110) surface, O<sub>br</sub> relaxes out of the surface with an expansion of the layer 1–2 O<sub>br</sub>-Mn5 spacing of +11% relative to the bulk (Table 3; see Figure 7b for a depiction of the layer sequence). Mn5 relaxes into the surface by –16%, while an

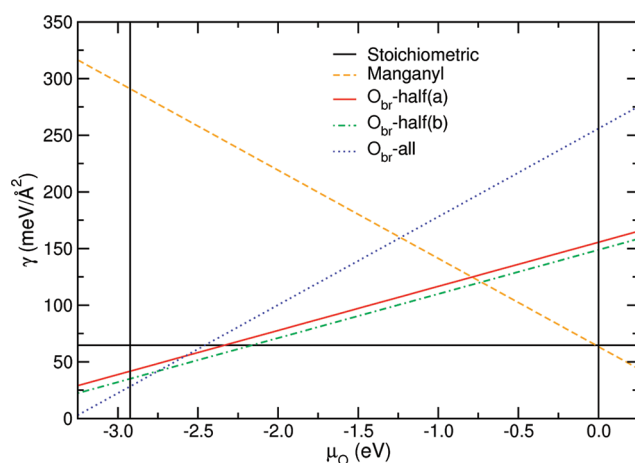


**Figure 8.** Surface free energies of various surface terminations of the  $\beta$ -MnO<sub>2</sub> (100) surface as determined by ab initio thermodynamics as a function of  $\mu_{\text{O}}$  at 0 K. The vertical black lines bracket the range of accessible  $\mu_{\text{O}}$  values as defined in the text.

expansion of the layer 3–4 spacing of +22% is observed. The outward relaxation of O<sub>br</sub> and inward relaxation of Mn5 have been predicted in a previous study using interatomic potentials.<sup>31</sup> A recent GGA study of the rutile TiO<sub>2</sub> (100) surface shows qualitative agreement with the vertical relaxations of the first three layers,<sup>35,75</sup> and small outward relaxation of O<sub>br</sub> and inward relaxation of layer 3 was calculated in an LDA study.<sup>76</sup> As shown in Table 4, Mn5 translates in the opposite direction as O<sub>br</sub>, layer 3 oxygen, and layer 4 oxygen along the [010] direction. These lateral relaxations coupled with the vertical relaxations result in Mn5 moving out of the same plane as the O<sub>br</sub> and layer 3 oxygen atoms. Lateral relaxations calculated for the rutile TiO<sub>2</sub> (100) surface in GGA<sup>75</sup> and LDA<sup>76</sup> studies show the same general trends, with Mn5 moving in the opposite direction as the oxygen atoms in its coordination sphere.

**A. Ab Initio Thermodynamics.** Like the (110) surface, the (100) surface can be reduced under oxygen-poor conditions (low  $p_{\text{O}_2}$  and high temperature), but oxidation of the surface may not be possible. Ab initio thermodynamics predicts that the (100) stoichiometric surface with a surface energy of 64.6 meV/Å<sup>2</sup> at 0 K is the most stable over the majority of the range of accessible  $\mu_{\text{O}}$  values (Figure 8), in agreement with an EELS study that found an average manganese valence of 4.0 at the surface of  $\beta$ -MnO<sub>2</sub>.<sup>26</sup> The oxidized surface (the manganyl surface; Figure 7c) becomes stable only at the oxygen-rich limit when  $\mu_{\text{O}}$  is above –0.016 eV (below 66 K at an ambient  $p_{\text{O}_2}$  of 0.2 bar), indicating that oxidation of the surface is unlikely. Reduction of the surface occurs by removing O<sub>br</sub>. At a  $\mu_{\text{O}}$  value of –2.16 eV, the O<sub>br</sub>-half(b) surface, formed by removing every other row of O<sub>br</sub> atoms (see Figure 7d), becomes more stable than the stoichiometric surface. This  $\mu_{\text{O}}$  value corresponds to a temperature of 1040 K in UHV (modeled with  $p_{\text{O}_2} = 10^{-10}$  bar). The surface with every other O<sub>br</sub> removed (O<sub>br</sub>-half(a)) is only 6.7 meV/Å<sup>2</sup> higher in  $\gamma$  than O<sub>br</sub>-half(b) at 0 K. It might therefore be possible to observe either of these surfaces, depending on the kinetics and the conditions under which reduction occurs. When  $\mu_{\text{O}}$  falls below –2.75 eV (the temperature is increased above 1310 K at a  $p_{\text{O}_2}$  of  $10^{-10}$  bar), all O<sub>br</sub> atoms can be removed from the surface to form O<sub>br</sub>-all (Figure 7e). These results show only thermodynamic stability at 0 K, and observed

surface reconstructions will depend on the method of surface preparation as well as oxygen partial pressure and temperature. As for the (110) surface, entropic contributions to  $\gamma$  at finite temperature lead to lower oxidation temperatures and higher reduction temperatures at a given  $p_{\text{O}_2}$  than indicated by  $\mu_{\text{O}}$  alone. For example, inclusion of these effects results in a predicted reduction temperature of 1090 K in UHV in the limiting case of oxygen vacancy concentrations of at least 50%. Additional details are described in the Supporting Information.

**B. Oxidized and Reduced Surface Reconstructions.** Although the stoichiometric surface is likely to be observed experimentally, interesting surface reconstructions are found when oxidation and reduction of the (100) surface are considered. Oxidation of the (100) surface results in the formation of manganyl groups with O–Mn5 bond lengths of 1.57 Å (the manganyl surface; Figure 7c). Analysis of the Mulliken and Hirshfeld spins indicate that Mn5 is oxidized to  $\text{Mn}^{\text{VI}}$  since there is approximately half of an unpaired electron in its d orbitals. Here, both electrons are drawn to the additional oxygen atom from Mn5 instead of from other atoms, as in the (110) manganyl surface. The greater extent of Mn5 oxidation in this case is likely due to the presence of two 2-fold coordinated oxygen ( $\text{O}_{\text{br}}$ ) in the Mn5 coordination sphere on the (100) surface, which take more electron density from Mn5 than the 3-fold coordinated oxygen in the Mn5 coordination sphere on the (110) surface. Similarly to the (110) surface, reduced surfaces contain high-spin  $\text{Mn}^{\text{III}}$ . On the  $\text{O}_{\text{br}}$ -half(a) surface, the Mn5 atoms are 4-fold coordinated high-spin  $\text{Mn}^{\text{III}}$ . Interestingly, all Mn5 on the surface are equivalent, in contrast to Mn6 on the (110)  $\text{O}_{\text{br}}$ -half(a) surface. As shown in Figure 7d, the  $\text{O}_{\text{br}}$ -half(b) surface consists of alternating rows of 4- and 5-fold coordinated Mn5 along the [010] direction. The 4-fold coordinated Mn5 undergo reduction to high-spin  $\text{Mn}^{\text{III}}$ , and layer 5 manganese are partially reduced to low-spin  $\text{Mn}^{\text{III}}$ . Surface relaxations for these (100) surfaces are given in the Supporting Information.

Under severely reducing conditions (low  $p_{\text{O}_2}$  and high temperature), it is predicted that all  $\text{O}_{\text{br}}$  atoms are removed from the surface ( $\text{O}_{\text{br}}$ -all; Figure 7e). Although this surface is unlikely to be observed outside the UHV chamber, it demonstrates the interesting relationship between the electronic structure of the surface manganese and surface reconstruction and is discussed in detail. Mn5 is reduced to high-spin  $\text{Mn}^{\text{III}}$ , as shown by the increase in magnitude of the spin on Mn5 by approximately 1.00 relative to the stoichiometric surface. Layer 5 manganese are reduced to low-spin  $\text{Mn}^{\text{III}}$  with spins an average of 0.18 higher than those calculated for the corresponding  $\text{Mn}(\text{H}_2\text{O})_x$  molecular complex with a formal 3+ oxidation state. This surface reconstruction proceeds by 3-fold coordinated, half-octahedral Mn5 falling into the surface so that it becomes nearly planar with layers 3 and 4 oxygen atoms and coordinates to a layer 6 oxygen (Figure 7e). The  $\text{O}_{\text{br}}$ -half(b) surface (Figure 7d) also reconstructs via the same mechanism. The inward relaxation of Mn5 translates to a layer 2–3 Mn5–O compression of –167% relative to the bulk and promotes expansion of the layer 3–4 spacing by +127% as well as considerable vertical relaxations deeper in the slab (Table 3). Large lateral relaxations along the [010] direction are experienced throughout the slab, especially for layers 2 and 3 (Table 4). These layers shift approximately –0.50 Å along the [010] direction to accommodate Mn5 as it relaxes into the surface. This surface reconstruction is not observed for the fully reduced rutile-type  $\text{SnO}_2$  (100) surface. Removal of all  $\text{O}_{\text{br}}$  atoms on that surface results in a SnO layer at

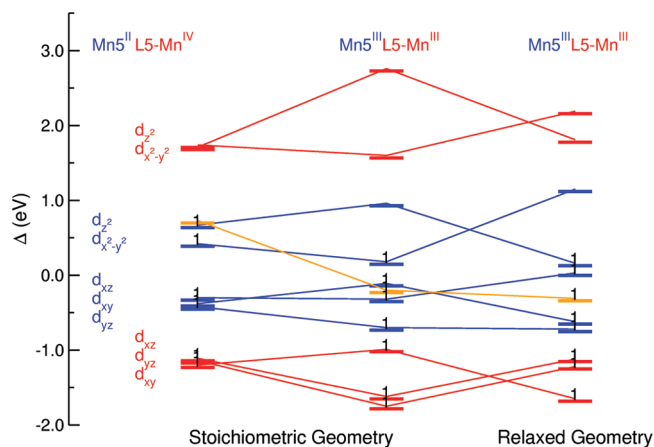


**Figure 9.** The difference in energies between the spin-up d orbitals and their average ( $\Delta$ ) for Mn5 and layer 5 manganese (L5-Mn) on the  $\beta$ - $\text{MnO}_2$  (100)  $\text{O}_{\text{br}}$ -all surface. The spin-down orbital shown in orange is the  $d_{xy}$  orbital for the initial and intermediate stages, and it is the  $d_{xz}$  orbital for the final geometry.

the surface with the tin atoms maintaining the 3-fold coordinated, half-octahedral geometry and with vertical relaxations similar to those of the bulk.<sup>35</sup>

The d-orbital picture for the first two layers of manganese atoms of  $\text{O}_{\text{br}}$ -all was examined to gain insight into the  $\text{O}_{\text{br}}$ -all reconstruction. First, it is noted that removal of one  $\text{O}_{\text{br}}$  per Mn5 from the stoichiometric surface initially results in high-spin  $\text{Mn}^{\text{II}}$  at the surface, as indicated by a Mulliken spin of –4.37 on Mn5. During relaxation, an electron is transferred from Mn5 to layer 5 manganese so that the first two layers of manganese atoms are reduced to  $\text{Mn}^{\text{III}}$ , as discussed previously. The question becomes whether the electron transfer drives surface reconstruction or surface reconstruction drives the electron transfer. To answer this question, the d-orbital energies were calculated for the molecular complexes representing Mn5 and layer 5 manganese before and after relaxation of  $\text{O}_{\text{br}}$ -all. For Mn5, 3+ and 2+ oxidation states were investigated for both initial and final geometries, and 4+ and 3+ oxidation states were examined for layer 5 manganese. The sum of the filled d-orbital  $\Delta$  values decreases significantly from –3.5 eV to –5.5 eV for electron transfer prior to reconstruction (see Figure 9). This large energy savings is not observed for the reconstruction step preceding electron transfer. Upon electron transfer, the  $e_g$  and  $t_{2g}$  orbitals on Mn5 and on layer 5 manganese split, leading to a decrease of 0.90 eV in the  $\Delta$  values of the filled  $t_{2g}$  orbitals on layer 5 manganese. The rest of the gain in energy is due to transfer of the Mn5  $d_{z^2}$  electron to the spin-down  $d_{xy}$  orbital on layer 5 manganese. No further decrease in the sum of the filled d-orbital  $\Delta$  values is observed upon surface reconstruction (Figure 9). The surface reconstruction at this point is driven by the relaxation of half-octahedral  $\text{Mn5}^{\text{III}}$  toward a highly stable trigonal planar geometry. Mn5 becomes 4-fold coordinated due to the proximity of layer 6 oxygen after relaxation. Electron transfer to layer 5 manganese thus occurs prior to relaxation of Mn5 into the surface. In summary, the  $\text{O}_{\text{br}}$ -all surface reconstruction illustrates the rich redox behavior of manganese and competition between manganese coordination geometry and steric and electrostatic constraints. This surface reconstruction is not observed for rutile-type  $\text{SnO}_2$  because tin is a  $d^{10}$  system and does not benefit from an adjustment in d-orbital occupations.

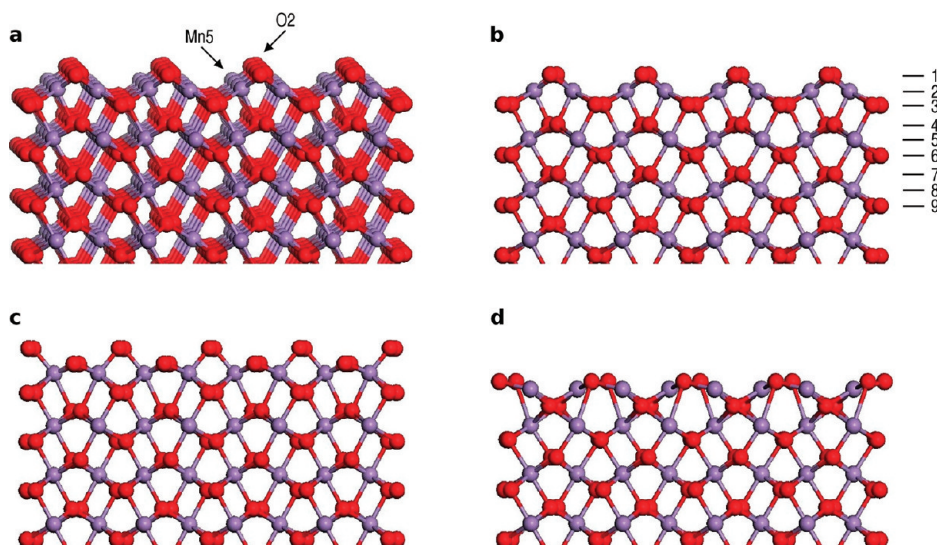


**Figure 10.** (a)  $\beta$ -MnO<sub>2</sub> (101) stoichiometric surface showing surface atom types; stable (101) surface terminations viewed along the  $[10\bar{1}]$  direction: (b) stoichiometric showing layer stacking sequence; (c) manganyl; (d) O2-all (O, red/dark sphere; Mn, purple/light sphere).

**Table 5.** Calculated Vertical Layer Spacings,  $d$  (Å), and Percent Relaxations with Respect to Theoretical Bulk Spacings for Selected Stable Surface Terminations of the  $\beta$ -MnO<sub>2</sub> (101) Surface

layers	stoichiometric		O2-all	
	$d$	% $\Delta$	$d$	% $\Delta$
1–2	0.781	+6		
2–3	0.669	−9	−0.360	−149
3–4	0.958	+1	1.173	+24
4–5	0.710	−4	0.949	+29
5–6	0.773	+5	0.694	−6
6–7	0.906	−4	0.838	−11
7–8	0.769	+4	0.813	+10
8–9	0.753	+2	0.767	+4

**3. (101) Surface.** The  $\beta$ -MnO<sub>2</sub> (101) stoichiometric surface differs from the (110) and (100) surface in that 2-fold coordinated oxygen atoms at the surface do not bridge manganese atoms in the same row (see Figure 10a). These oxygen atoms are thus denoted O2, and the surface manganese are 5-fold coordinated Mn5. The Mulliken and Hirshfeld spins on Mn5 are 2.44 and 2.28, respectively, in agreement with the spins on Mn5 on the (110) and (100) surfaces and indicative of high-spin Mn<sup>IV</sup> by comparison with the bulk values. Relative to the bulk, the layer 1–2 O2–Mn5 spacing undergoes an expansion of +6% (Table 5; see Figure 10b for layer sequencing). Mn5 relaxes into the surface by −9%. These vertical relaxations are similar to those observed in GGA studies<sup>35,54,63</sup> of the rutile-type SnO<sub>2</sub> (101) surface although not as large. Calculations performed using interatomic pair potentials<sup>31</sup> show different directions for the vertical relaxations, probably because the treatment of electronic structure in the present study is important in predicting surface reconstructions, as shown earlier. Lateral relaxations along both the  $[10\bar{1}]$  and  $[010]$  directions are observed (Table 6). Along the

**Table 6.** Calculated Lateral Relaxations (Å) with Respect to Theoretical Bulk Positions for Selected Stable Surface Terminations of the  $\beta$ -MnO<sub>2</sub> (101) Surface

layers	stoichiometric		O2-all	
	$[10\bar{1}]$	$[010]$	$[10\bar{1}]$	$[010]$
1	+0.05	±0.08		
2	−0.08	±0.18	−0.63	±0.02
3	−0.04	±0.04	−0.46	±0.16
4	+0.02	±0.05	+0.38	±0.47
5	0	±0.06	+0.02	±0.01
6	−0.04	±0.04	−0.09	±0.20
7	+0.02	±0.03	+0.13	±0.12
8	−0.01	±0.02	+0.01	±0.02
9	−0.03	±0.03	−0.06	±0.09
10	+0.03	±0.04	+0.06	±0.07

$[010]$  direction, atoms in the same layer move toward each other. This translation is most noticeable for Mn5 and can be seen in Figure 10b.

**A. Ab Initio Thermodynamics.** Ab initio thermodynamics was used to predict the relative stability of the (101) stoichiometric surface and four oxidized or reduced surfaces. As with the (110) and (100) surfaces, the stoichiometric surface with  $\gamma = 79.7$  meV/Å<sup>2</sup> at 0 K is the most stable surface termination over a wide range of  $\mu_{\text{O}}$  (Figure 11). The manganese valence of 4.0 at this surface is consistent with the experimental value found for  $\beta$ -MnO<sub>2</sub>.<sup>26</sup> An oxidized surface on which Mn5 becomes octahedral (the manganyl surface; Figure 10c) is more stable than the stoichiometric surface above a  $\mu_{\text{O}}$  value of −0.10 eV, which corresponds to a temperature of 135 K at ambient  $p_{\text{O}_2}$  (0.2 bar). The (101) surface becomes fully reduced by removal of all O2 atoms at a  $\mu_{\text{O}}$  value of −2.12 eV (O2-all; Figure 10d). The surface reconstruction with every other row of O2 atoms removed (O2-half(b)) is only 2.2 meV/Å<sup>2</sup> higher in energy than

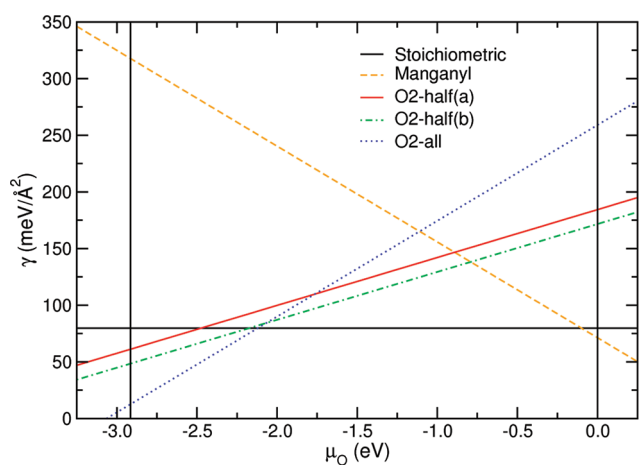


**Figure 11.** Surface free energies of various surface terminations of the  $\beta$ - $\text{MnO}_2$  (101) surface as determined by ab initio thermodynamics as a function of  $\mu_{\text{O}}$  at 0 K. The vertical black lines bracket the range of accessible  $\mu_{\text{O}}$  values as defined in the text.

O2-all at  $-2.12$  eV. At 0 K,  $12.7 \text{ meV}/\text{\AA}^2$  separates the O2-half(b) and O2-half(a) surfaces, the latter of which is obtained by removing every other O2 atom. The  $\mu_{\text{O}}$  value at which reduction occurs ( $-2.12$  eV) translates to a temperature of 1021 K at a  $p_{\text{O}_2}$  of  $10^{-10}$  bar (UHV conditions) and is significantly higher than the experimental decomposition temperature (808 K).<sup>69</sup> Again, comparison between the calculated and experimental decomposition temperatures is made cautiously, given the limiting case of 100% O2 vacancies and neglect of kinetic factors in the calculations. Kinetic limitations to the formation of the oxidized or reduced surfaces may affect which surface is observed experimentally when different surface preparation techniques and temperature and pressure conditions are used. The temperature range over which the stoichiometric surface can be observed is predicted to expand when entropic contributions to  $\gamma$  are considered, as is the case for the (110) and (100) surfaces. Specific examples at ambient and UHV conditions are given the Supporting Information.

**B. Oxidized and Reduced Surface Reconstructions.** Although the oxidized and reduced surfaces are not relevant under typical UHV conditions, they may play a role in applications where other strong redox agents are present (e.g., heavy metal ions in the environment). For all surfaces considered, a general description of the electronic structure of the surface manganese is given, and structural information in the form of surface relaxations can be found in the Supporting Information. Near oxygen-rich limiting conditions, manganyl groups with bond lengths of  $1.59$ – $1.60$  Å form on the (101) surface (the manganyl surface; Figure 10c). Oxidation of Mn5 leads to manganese atoms with Mulliken spins of  $0.96$  and  $-0.64$  at the surface. These spins indicate the presence of an unpaired d electron on Mn5 and lead to the assignment of a 6+ oxidation state to Mn5, as is the case for Mn5 on the (100) manganyl surface. The small differences in spin magnitude suggest reduced symmetry of the surface; yet, the differences in geometry around the inequivalent Mn5 atoms are insignificant. As with the (110) and (100) reduced surfaces, Mn5 favors the formation of high-spin  $\text{Mn}^{\text{III}}$ . The O2-half(a) surface consists of 4-fold coordinated manganese atoms. Like the (110)  $\text{O}_{\text{br}}$ -quarter and  $\text{O}_{\text{br}}$ -half(a) surfaces, the symmetry of the surface must be broken to find a true minimum-energy structure. Half of

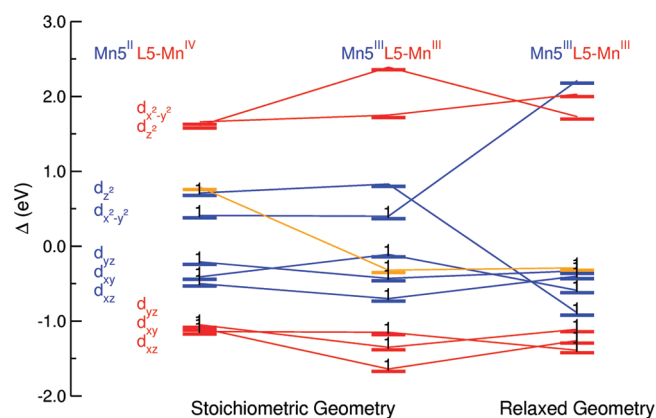


**Figure 12.** The difference in energies between the spin-up d orbitals and their average ( $\Delta$ ) for Mn5 and layer 5 manganese (L5-Mn) on the  $\beta$ - $\text{MnO}_2$  (101) O2-all surface. The spin-down orbital shown in orange is the  $d_{xz}$  orbital for the initial and intermediate stages, and it is the  $d_{xy}$  orbital for the final geometry.

the Mn5 atoms are reduced to high-spin  $\text{Mn}^{\text{III}}$ , and additional electron density is delocalized among half of the layer 5 manganese atoms. On the O2-half(b) surface, rows of 4- and 5-fold coordinated Mn5 alternate along the [010] direction. All of the 4-fold coordinated and half of the 5-fold coordinated Mn5 are high-spin  $\text{Mn}^{\text{III}}$ .

On the basis of the ab initio thermodynamics calculations, the most likely surface reconstruction to be observed under severely reducing conditions (low  $p_{\text{O}_2}$  and high temperature) is O2-all (Figure 10d). 3-Fold coordinated, half-octahedral Mn5 are present at the surface initially. Relaxation of the slab is driven by reduced Mn5 rearranging to the more favorable square planar  $\text{Mn}^{\text{III}}$ . Layer 5 manganese atoms are reduced to low-spin  $\text{Mn}^{\text{III}}$  with an average decrease in their spins by  $0.40$ . As Mn5 relaxes into the surface by  $-149\%$  (Table 5), the layer 3 oxygen atoms become the topmost layer (see Figure 10d). The layer 3–4 and 4–5 spacings expand by  $+24\%$  and  $+29\%$  relative to the bulk, respectively. These vertical relaxations differ considerably from those calculated for the rutile-type  $\text{SnO}_2$  (101) reduced surface because the reduced  $\text{SnO}_2$  reconstruction maintains a structure similar to the stoichiometric surface.<sup>35,54,63</sup> The reconstruction predicted here has not yet been observed in rutile-type structures, probably because the well-studied surfaces have either filled or completely empty d bands. In the O2-all surface, all layers experience lateral relaxations (Table 6), with translation of atoms in the same layer toward each other along the [010] direction, except for layers containing manganese and layer 3, where the atoms move away from each other. Significant relaxation of the first three layers along the  $[10\bar{1}]$  direction aids the formation of square planar Mn5. Given the studies on fully relaxed  $\text{Mn}(\text{H}_2\text{O})_x$  molecular complexes discussed previously, the driving force for this surface reconstruction is likely related to the high stability of  $\text{Mn}^{\text{III}}$  square planar complexes.

Investigation of the d-orbital energies for the first two layers of manganese atoms supports the proposed driving force for the O2-all surface reconstruction. Interestingly, this reconstruction occurs through essentially the same mechanism as that for the (100)  $\text{O}_{\text{br}}$ -all surface. Prior to relaxation, the O2-all surface is calculated to have high-spin  $\text{Mn}^{\text{II}}$  at the surface. Transfer of one electron from Mn5 to the layer 5 manganese leads to high-spin  $\text{Mn}^{\text{III}}$  and low-spin  $\text{Mn}^{\text{III}}$  in layers 2 and 5, respectively. Then

Mn5 relaxes to the square planar geometry. Figure 12 illustrates the changes in the  $\Delta$  values of the spin-up d orbitals as the surface reconstruction progresses through the stages outlined above. The electron transfer from the spin-up  $d_{z^2}$  orbital on Mn5 to the spin-down  $d_{xz}$  orbital on layer 5 manganese results in a 1.0 eV energy savings. Another energetically favorable change is the splitting of the  $t_{2g}$  and  $e_g$  orbitals on layer 5 manganese as measured by the d-orbital  $\Delta$  values. The sum of the filled d-orbital  $\Delta$  values decreases by a total of 2.0 eV upon electron transfer. Unlike the (100)  $O_{br}$ -all reconstruction, relaxation of the slab leads to a significant lowering of the sum of the filled d-orbital  $\Delta$  values by an additional 0.98 eV. This energetic change arises mostly from the large decrease in the  $\Delta$  value of the Mn5  $d_{z^2}$  orbital, to which the Mn5  $d_{x^2-y^2}$  electron is transferred upon relaxation. These results agree with the predicted stability of square planar  $Mn^{III}$  discussed previously and demonstrate how d-orbital occupancy can drive surface reconstructions for transition metal oxides.

**4. Comparison of (110), (100), and (101) Surfaces.** In agreement with previous GGA studies,<sup>35,38,70</sup> the stability of the stoichiometric  $\beta$ - $MnO_2$  surfaces ranks as follows in order of decreasing stability: (110) > (100) > (101). The surface free energies at 298.15 K are 47.2, 57.5, and 76.0 meV/ $\text{\AA}^2$  for the (110), (100), and (101) surfaces, respectively. On the basis of the  $\mu_O$  value at which the stoichiometric surface transforms into the manganyl surface at 0 K, the (110) surface is the most easily oxidized surface, followed by the (101) surface, and then the (100) surface. This transition occurs at  $-0.17$  eV for the (110) surface,  $-0.10$  eV for the (101) surface, and  $-0.016$  eV for the (100) surface. Because these  $\mu_O$  values correspond to temperatures less than 200 K under ambient  $p_{O_2}$ ,  $\beta$ - $MnO_2$  surfaces are probably not oxidized at experimentally relevant conditions. Comparing the reducibilities of the surfaces is less straightforward, since the oxygen vacancy concentration at which reduction is first predicted to occur is not the same for the three surfaces. For a more equal comparison, the  $\mu_O$  values for the transition from the stoichiometric surface to the fully reduced surface are employed. The (101) surface is easiest to fully reduce as the  $O_2$ -all surface becomes the most stable surface at  $\mu_O = -2.12$  eV. The (110) surface follows with  $\gamma$  of the  $O_s$ -all and  $O_s$ -half/ $O_{br}$ -all surfaces falling below that of the stoichiometric surface at a  $\mu_O$  value of  $-2.33$  eV. The (100) surface is predicted to go from the stoichiometric surface termination to  $O_{br}$ -all at  $-2.46$  eV. In UHV (modeled with  $p_{O_2} = 10^{-10}$  bar), these  $\mu_O$  values translate to temperature thresholds of 1020, 1120, and 1180 K for the (101), (110), and (100) surfaces, respectively. When entropic effects are included in the calculation of  $\gamma$  at finite temperature, these temperatures increase by at least 80 K, but the relative reducibilities of the surfaces remain unchanged. A GGA study of rutile-type  $SnO_2$  surfaces concluded that the (101) surface was the most easily reduced, followed by the (100) and then the (110) surfaces,<sup>35</sup> in agreement with a previous study of the (101) and (110) surfaces.<sup>63</sup> It should be noted that partial reduction of these surfaces may produce a different ordering for their reducibilities.

## CONCLUSIONS

Ab initio thermodynamics have been used to investigate stable  $\beta$ - $MnO_2$  surfaces and their redox behavior. The predicted stability of the (110), (100), and (101) stoichiometric surfaces follows the trends previously determined for rutile  $TiO_2$  and rutile-type  $SnO_2$ : (110) > (100) > (101). Generally, the

stoichiometric surfaces are predicted to be observed under environmentally relevant conditions, in agreement with experiments that found a manganese valence of 4.0 at the  $\beta$ - $MnO_2$  surface.<sup>26</sup> Fourteen oxidized or reduced surfaces were examined for the (110) surface, and four oxidized or reduced surfaces of the (100) and (101) surfaces were studied. Oxidation of the (110), (100), and (101) surfaces results in the formation of manganyl groups at the surface. The surface energies for these oxidized surfaces indicate that the (110) and (101) surfaces may be oxidized under oxygen-rich, low-temperature conditions (below 194 and 118 K, respectively, at ambient  $p_{O_2}$  when entropic effects are included). It is unlikely, however, that the (100) surface can be oxidized.

It has been predicted that the (110), (100), and (101) surfaces are reduced at low  $p_{O_2}$  and high temperature (above 1000 K at  $p_{O_2} = 10^{-10}$  bar), forming interesting surface reconstructions that have not been observed for other rutile-type metal oxides. In most cases, these reconstructions demonstrate the preference of  $Mn^{III}$  for certain coordination geometries, especially the square planar configuration. Over the range of accessible  $\mu_O$  values, seven (110) reduced surfaces have surface energies lower than that of the stoichiometric surface. These surfaces involve mostly removal of  $O_{br}$  atoms. Surfaces missing  $O_s$  atoms are stable only if enough  $O_s$  atoms are removed to allow for significant surface reconstructions. Under severely reducing conditions, the (110)  $O_s$ -all and  $O_s$ -half/ $O_{br}$ -all surfaces are the most thermodynamically stable. The (100) and (101) surfaces are predicted to exhibit two or one reduced surface, respectively. On the (100) and (101) fully reduced surfaces, Mn5 undergoes significant relaxation into the surface, which is not observed for similar  $SnO_2$  surfaces, due to the absence of a partially filled d band in the latter cases.

The extra electrons on  $\beta$ - $MnO_2$  reduced surfaces typically localize to surface manganese, forming  $Mn^{III}$  at the surface. For the (110)  $O_{br}$ -quarter,  $O_{br}$ -all,  $O_s$ -all, and  $O_s$ -half/ $O_{br}$ -all and the (101)  $O_2$ -half(a) surfaces, some of the additional electron density delocalizes among subsurface atoms. In a few cases, breaking the symmetry of the surface allows an electron to localize to one surface manganese atom, producing multiple manganese oxidation states at the surface. These surface reconstructions ((110)  $O_{br}$ -quarter and  $O_{br}$ -half(a) and (101)  $O_2$ -half(a)) are driven by the Jahn–Teller distortion of the  $d^4$   $Mn^{III}$  coordination geometry. These results demonstrate the importance of vibrational analysis since the lower-energy, asymmetric surfaces would not have been located without perturbing the metastable symmetric surface along the dominant imaginary frequency.

Because of the directionality of the d orbitals, the thermodynamically stable reduced surfaces exhibit manganese coordination geometries with the d electrons occupying lower energy states. Detailed electronic structure analysis was performed to explain the role of d-orbital occupations and coordination geometry in producing the new surface reconstructions predicted here. This type of analysis illustrates that the redox behavior of manganese oxides may involve significant structural aspects to consider, for example, in modeling their role in heavy metal oxidation. In the present study, the electronic structure of surface manganese is intimately related to the reconstructions predicted. The (110)  $O_s$ -half surface reconstruction is driven by the stability of square planar  $Mn^{III}$ . For the (110)  $O_s$ -half/ $O_{br}$ -all surface, however, steric and electrostatic interactions prevent simple relaxation to the most stable  $Mn^{III}$  or  $Mn^{II}$  coordination geometry. Mn5 and Mn6 relax toward trigonal planar coordination

geometries, but they become too close to each other and experience repulsion. In the end, Mn5 adopts a tetrahedral geometry, which is unfavorable for Mn<sup>III</sup>, while Mn6 becomes octahedrally coordinated. The (100) O<sub>br</sub>-all and (101) O<sub>2</sub>-all surfaces result from the energetically favorable electron transfer from a d orbital on the surface manganese to a d orbital on subsurface manganese. The surface manganese atoms then relax into the surface toward more stable trigonal planar and square planar geometries for the (100) and (101) reduced surfaces, respectively. These new reconstructions thus arise from the complex interplay between finding optimal d-orbital occupation and manganese coordination geometry and optimizing steric and electrostatic interactions. Due to the lack of surface studies on  $\beta$ -MnO<sub>2</sub>, the surface reconstructions presented here are predictive. These results illustrate rich structural possibilities and redox behavior of  $\beta$ -MnO<sub>2</sub> surfaces, which could be important in catalytic and sensing applications as well as in oxidation of heavy metals in the environment. Experimental validation of these remarkable surface reconstructions might help to develop an understanding of the role of these surfaces in the complex processes in which they participate.

## ■ ASSOCIATED CONTENT

**S Supporting Information.** Surface relaxations for the (110), (100), and (101) surface terminations discussed in the text, finite-temperature ab initio thermodynamics results, and discussion of partial density of states calculations. This information is available free of charge via the Internet at <http://pubs.acs.org>.

## ■ AUTHOR INFORMATION

### Corresponding Author

\*E-mail: [gloria.oxford@nist.gov](mailto:gloria.oxford@nist.gov).

## ■ ACKNOWLEDGMENT

GAEO was supported by the National Research Council. This work utilized high-performance computing resources of the Raritan cluster at the National Institute of Standards and Technology and of the Arctic Region Supercomputing Center at the University of Alaska Fairbanks. The authors thank Profs. Sara Mason and Tom Trainor and Drs. Peter Eng and Joanne Stubbs for useful discussions.

## ■ REFERENCES

- (1) Post, J. E. *Proc. Natl. Acad. Sci. U.S.A.* **1999**, *96*, 3447.
- (2) Balachandran, D.; Morgan, D.; Ceder, G.; van de Walle, A. *J. Solid State Chem.* **2003**, *173*, 462.
- (3) Cao, Y. L.; Yang, H. X.; Ai, X. P.; Xiao, L. F. *J. Electroanal. Chem.* **2003**, *557*, 127.
- (4) Ivanova, N. D.; Ivanov, S. V.; Boldyrev, E. I.; Sokol'skii, G. V.; Makeeva, I. S. *Russ. J. Appl. Chem.* **2002**, *75*, 1420.
- (5) Han, Y. F.; Chen, L.; Ramesh, K.; Widjaja, E.; Chilukoti, S.; Surjami, I. K.; Chen, J. *J. Catal.* **2008**, *253*, 261.
- (6) Tang, X. F.; Li, J. H.; Sun, L. A.; Hao, J. M. *Appl. Catal., B* **2010**, *99*, 156.
- (7) Liu, D.; Sansalone, J. J.; Cartledge, F. K. *J. Environ. Eng.* **2005**, *131*, 1178.
- (8) Ahammed, M. M.; Meera, V. *J. Hazard. Mater.* **2010**, *181*, 788.
- (9) Cao, X.; Wang, N.; Wang, L.; Mo, C.; Xu, Y.; Cai, X.; Guo, L. *Sens. Actuators, B* **2010**, *147*, 730.
- (10) Eary, L. E.; Rai, D. *Environ. Sci. Technol.* **1987**, *21*, 1187.

- (11) Johnson, C. A.; Xyla, A. G. *Geochim. Cosmochim. Acta* **1991**, *55*, 2861.
- (12) Fendorf, S. E.; Fendorf, M.; Sparks, D. L.; Gronsky, R. J. *Colloid Interface Sci.* **1992**, *153*, 37.
- (13) Fendorf, S. E.; Zamoski, R. J. *Environ. Sci. Technol.* **1992**, *26*, 79.
- (14) Manceau, A.; Charlet, L. *J. Colloid Interface Sci.* **1992**, *148*, 425.
- (15) Silvester, E.; Charlet, L.; Manceau, A. *J. Phys. Chem.* **1995**, *99*, 16662.
- (16) Nico, P. S.; Zamoski, R. J. *Environ. Sci. Technol.* **2000**, *34*, 3363.
- (17) Weaver, R. M.; Hochella, M. F.; Ilton, E. S. *Geochim. Cosmochim. Acta* **2002**, *66*, 4119.
- (18) Nesbitt, H. W.; Canning, G. W.; Bancroft, G. M. *Geochim. Cosmochim. Acta* **1998**, *62*, 2097.
- (19) Chiu, V. Q.; Hering, J. G. *Environ. Sci. Technol.* **2000**, *34*, 2029.
- (20) Manning, B. A.; Fendorf, S. E.; Bostick, B.; Suarez, D. L. *Environ. Sci. Technol.* **2002**, *36*, 976.
- (21) Foster, A. L.; Brown, G. E.; Parks, G. A. *Geochim. Cosmochim. Acta* **2003**, *67*, 1937.
- (22) Zhu, M. Q.; Paul, K. W.; Kubicki, J. D.; Sparks, D. L. *Environ. Sci. Technol.* **2009**, *43*, 6655.
- (23) Oku, M.; Hirokawa, K.; Ikeda, S. *J. Electron Spectrosc. Relat. Phenom.* **1975**, *7*, 465.
- (24) Foord, J. S.; Jackman, R. B.; Allen, G. C. *Philos. Mag. A* **1984**, *49*, 657.
- (25) Langell, M. A.; Hutchings, C. W.; Carson, G. A.; Nassir, M. H. *J. Vac. Sci. Technol., A* **1996**, *14*, 1656.
- (26) Loomer, D. B.; Al, T. A.; Weaver, L.; Cogswell, S. *Am. Mineral.* **2007**, *92*, 72.
- (27) Chambers, S. A.; Liang, Y. *Surf. Sci.* **1999**, *420*, 123.
- (28) Xing, X. J.; Yu, Y. P.; Xu, L. M.; Wu, S. X.; Li, S. W. *J. Phys. Chem. C* **2008**, *112*, 15526.
- (29) Franchini, C.; Bayer, V.; Podloucky, R.; Parteder, G.; Surney, S.; Netzer, F. P. *Phys. Rev. B* **2006**, *73*, 155402.
- (30) Xia, S. W.; Pan, G.; Cai, Z. L.; Wang, Y.; Reimers, J. R. *J. Phys. Chem. C* **2007**, *111*, 10427.
- (31) Maphanga, R. R.; Parker, S. C.; Ngoepe, P. E. *Surf. Sci.* **2009**, *603*, 3184.
- (32) Brown, G. E.; Trainor, T. P.; Chaka, A. M. In *Chemical Bonding at Surfaces and Interfaces*; Nilsson, A., Pettersson, L. G. M., Norskov, J., Eds.; Elsevier: New York, 2008; p 457.
- (33) Wang, X. G.; Weiss, W.; Shaikhutdinov, S. K.; Ritter, M.; Petersen, M.; Wagner, F.; Schlogl, R.; Scheffler, M. *Phys. Rev. Lett.* **1998**, *81*, 1038.
- (34) Reuter, K.; Scheffler, M. *Phys. Rev. B* **2002**, *65*, 035406.
- (35) Batzill, M.; Katsiev, K.; Burst, J. M.; Diebold, U.; Chaka, A. M.; Delley, B. *Phys. Rev. B* **2005**, *72*, 165414.
- (36) Kiejna, A.; Pabisiak, T.; Gao, S. W. *J. Phys.: Condens. Matter* **2006**, *18*, 4207.
- (37) Lo, C. S.; Tanwar, K. S.; Chaka, A. M.; Trainor, T. P. *Phys. Rev. B* **2007**, *75*, 075425.
- (38) Perron, H.; Domain, C.; Roques, J.; Drot, R.; Simoni, E.; Catalette, H. *Theor. Chem. Acc.* **2007**, *117*, 565.
- (39) Mason, S. E.; Iceman, C. R.; Trainor, T. P.; Chaka, A. M. *Phys. Rev. B* **2010**, *81*, 125423.
- (40) Bolzan, A. A.; Fong, C.; Kennedy, B. J.; Howard, C. J. *Aust. J. Chem.* **1993**, *46*, 939.
- (41) Perdew, J. P.; Burke, K.; Ernzerhof, M. *Phys. Rev. Lett.* **1996**, *77*, 3865.
- (42) Delley, B. *J. Chem. Phys.* **1990**, *92*, 508.
- (43) Delley, B. *J. Chem. Phys.* **2000**, *113*, 7756.
- (44) Mention of commercial software in this paper does not imply approval or endorsement by NIST, nor does it imply that such software is necessarily the best available for the purpose.
- (45) Monkhorst, H. J.; Pack, J. D. *Phys. Rev. B* **1976**, *13*, 5188.
- (46) Yoshimori, A. *J. Phys. Soc. Jpn.* **1959**, *14*, 807.
- (47) Sato, H.; Enoki, T.; Isobe, M.; Ueda, Y. *Phys. Rev. B* **2000**, *61*, 3563.
- (48) Balachandran, D.; Morgan, D.; Ceder, G. *J. Solid State Chem.* **2002**, *166*, 91.

- (49) Franchini, C.; Podloucky, R.; Paier, J.; Marsman, M.; Kresse, G. *Phys. Rev. B* **2007**, *75*, 195128.
- (50) Sherman, D. M. *Geochim. Cosmochim. Acta* **2005**, *69*, 3249.
- (51) Anisimov, V. I.; Zaanen, J.; Andersen, O. K. *Phys. Rev. B* **1991**, *44*, 943.
- (52) Crocombette, J. P.; Torumba, D.; Chartier, A. *Phys. Rev. B* **2011**, *83*, 185107.
- (53) Dorado, B.; Jomard, G.; Freyss, M.; Bertolus, M. *Phys. Rev. B* **2010**, *82*, 035114.
- (54) Batzill, M.; Chaka, A. M.; Diebold, U. *Europhys. Lett.* **2004**, *65*, 61.
- (55) Rohrbach, A.; Hafner, J.; Kresse, G. *Phys. Rev. B* **2004**, *70*, 125426.
- (56) Lemire, C.; Bertarione, S.; Zecchina, A.; Scarano, D.; Chaka, A.; Shaikhutdinov, S.; Freund, H. J. *Phys. Rev. Lett.* **2005**, *94*, 166101.
- (57) Prosandeev, S. A.; Cockayne, E.; Burton, B. P.; Kamba, S.; Petzelt, J.; Yuzyuk, Y.; Katiyar, R. S.; Vakhrushev, S. B. *Phys. Rev. B* **2004**, *70*, 134110.
- (58) Wang, X. G.; Chaka, A.; Scheffler, M. *Phys. Rev. Lett.* **2000**, *84*, 3650.
- (59) Stampfl, C.; Ganduglia-Pirovano, M. V.; Reuter, K.; Scheffler, M. *Surf. Sci.* **2002**, *500*, 368.
- (60) Reuter, K.; Scheffler, M. *Phys. Rev. B* **2003**, *68*, 045407.
- (61) Reuter, K.; Scheffler, M. *Phys. Rev. Lett.* **2003**, *90*, 046103.
- (62) Sun, Q.; Reuter, K.; Scheffler, M. *Phys. Rev. B* **2003**, *67*, 205424.
- (63) Bergermayer, W.; Tanaka, I. *Appl. Phys. Lett.* **2004**, *84*, 909.
- (64) Trainor, T. P.; Chaka, A. M.; Eng, P. J.; Newville, M.; Waychunas, G. A.; Catalano, J. G.; Brown, G. E. *Surf. Sci.* **2004**, *573*, 204.
- (65) Negreira, A. S.; Aboud, S.; Wilcox, J. *Phys. Rev. B* **2011**, *83*, 045423.
- (66) Hobbs, D.; Hafner, J.; Spisak, D. *Phys. Rev. B* **2003**, *68*, 014407.
- (67) NIST-JANAF Thermochemical Tables, 4th ed.; Chase, J., Ed.; American Chemical Society: Washington, DC, 1998.
- (68) Robie, R. A.; Hemingway, B. S. *J. Chem. Thermodyn.* **1985**, *17*, 165.
- (69) *CRC Handbook of Chemistry and Physics*; 86th ed.; CRC Press: Boca Raton, FL, 2005.
- (70) Morgan, B. J.; Watson, G. W. *J. Phys. Chem. C* **2009**, *113*, 7322.
- (71) Charlton, G.; Howes, P. B.; Nicklin, C. L.; Steadman, P.; Taylor, J. S. G.; Murny, C. A.; Harte, S. P.; Mercer, J.; McGrath, R.; Norman, D.; Turner, T. S.; Thornton, G. *Phys. Rev. Lett.* **1997**, *78*, 495.
- (72) Lindsay, R.; Wander, A.; Ernst, A.; Montanari, B.; Thornton, G.; Harrison, N. M. *Phys. Rev. Lett.* **2005**, *94*, 246102.
- (73) Bates, S. P.; Kresse, G.; Gillan, M. J. *Surf. Sci.* **1997**, *385*, 386.
- (74) Bandura, A. V.; Sykes, D. G.; Shapovalov, V.; Troung, T. N.; Kubicki, J. D.; Evarestov, R. A. *J. Phys. Chem. B* **2004**, *108*, 7844.
- (75) Kamisaka, H.; Yamashita, K. *Surf. Sci.* **2007**, *601*, 4824.
- (76) Ramamoorthy, M.; Vanderbilt, D.; King-Smith, R. D. *Phys. Rev. B* **1994**, *49*, 16721.
- (77) Diebold, U. *Surf. Sci. Rep.* **2003**, *48*, 53.
- (78) Jarvis, E. A.; Chaka, A. M. *Surf. Sci.* **2007**, *601*, 1909.
- (79) Cotton, F. A.; Wilkinson, G.; Murillo, C. A.; Bochmann, M. *Advanced Inorganic Chemistry*, 6th ed.; John Wiley & Sons, Inc.: New York, 1999.